Optimizing Micro-vortex Chamber for Living Single Cell Rotation

by

Wenjie Zhang

A Thesis Presented in Partial Fulfillment
of the Requirements for the Degree
Master of Science

Approved April 2011 by the
Graduate Supervisory Committee:

David Frakes, Co-Chair
Deirdre Meldrum, Co-Chair
Shih-Hui Chao
Xiao Wang

ARIZONA STATE UNIVERSITY

May 2011

ABSTRACT

Single cell phenotypic heterogeneity studies reveal more information about the pathogenesis process than conventional bulk methods. Furthermore, investigation of the individual cellular response mechanism during rapid environmental changes can only be achieved at single cell level. By enabling the study of cellular morphology, a single cell three-dimensional (3D) imaging system can be used to diagnose fatal diseases, such as cancer, at an early stage. One proven method, CellCT, accomplishes 3D imaging by rotating a single cell around a fixed axis. However, some existing cell rotating mechanisms require either intricate microfabrication, and some fail to provide a suitable environment for living cells. This thesis develops a microvorterx chamber that allows living cells to be rotated by hydrodynamic alone while facilitating imaging access.

In this thesis work, 1) the new chamber design was developed through numerical simulation. Simulations revealed that in order to form a microvortex in the side chamber, the ratio of the chamber opening to the channel width must be smaller than one. After comparing different chamber designs, the trapezoidal side chamber was selected because it demonstrated controllable circulation and met the imaging requirements. Microvortex properties were not sensitive to the chambers with interface angles ranging from 0.32 to 0.64. A similar trend was observed when chamber heights were larger than chamber opening. 2) Micro-particle image velocimetry was used to characterize microvortices and validate simulation results. Agreement between experimentation and simulation confirmed

that numerical simulation was an effective method for chamber design. 3) Finally, cell rotation experiments were performed in the trapezoidal side chamber. The experimental results demonstrated cell rotational rates ranging from 12 to 29 rpm for regular cells. With a volumetric flow rate of 0.5 μL/s, an irregular cell rotated at a mean rate of 97 ± 3 rpm. Rotational rates can be changed by altering inlet flow rates.

TABLE OF CONTENTS

Page

LIST OF FIGURES

Figure Page

LIST OF TABLES

Table Page

Chapter 1

SPECIFIC AIMS

Cell CT facilitates three dimensional (3D) cellular images with isotropic resolution, and it is able to detect fatal diseases at an early stage by comparing the cellular morphology with acknowledged databases. Cell CT system constructs 3D images by taking projections from many angles around a single cell while rotating. However, previous cell rotation devices suffered from imaging distortion problems, and failed to provide biocompatible media for living cells. To address those disadvantages, the new cell rotation device must allow living cells to be imaged in real time with a flat surface. The concept of microvortex-based manipulation allows a single cell to rotate free in media, and it was adapted in this study with the added requirement of properly configured optical access. In this thesis work, development of a microvortex-based single cell rotation device with a flat side surface for imaging was achieved through the following aims.

Aim 1: Apply computational fluid dynamics (CFD) to facilitate chamber design

The goal of this aim was to simulate the flows of various side chambers for selection of the best design. The flow profile inside of a microvortex system has not been fully discussed by previous studies. It is clear that not all side chambers are capable of forming microvortices, and some of them do not meet the aforementioned imaging requirements. Therefore, CFD was applied to achieve the flowing sub-aims:

- Investigate the factors that affect microvortex formation
- Evaluate side chambers with different geometries

- Optimize performance by altering design parameters

Aim 2: Experimental verification with micro particle-image velocimetry (μ-PIV)

The goal of this aim was to verify the performance of the fabricated microfluidic device by using μ-PIV. The final design selected from the CFD simulations was fabricated by standard soft lithography. It is commonly acknowledged that fluidic behaviors under micro scales may show different phenomena than those on macro scales or from numerical simulation. Based on reviews of the existing literature, it is clear that secondary recirculation flow profiles in the side chamber have not been adequately quantified using experimental methods. Therefore, μ-PIV was employed to quantify the fluidic profile, and then compare with CFD.

Aim 3: Rotate a single cell with the optimized chamber design

The purpose of this aim was to validate the ability of the new side chamber to rotate a sing cell. In order to build a 3D image, projections from multiple angles must be acquired. In this case, the cell must be rotated around a fixed axis at a moderate rate, since the objective lens is fixed on a stage. Validation of the new chamber was performed thorough the following sub-aims:

- Rotate a polystyrene particle
- Rotate a spherical cell
- Rotate an irregularly shaped cell

Chapter 2

INTRODUCTION

2.1 Single cell analysis with multiple perspectives imaging

Studies at the single cell level become an important new frontier for cell biology and microbiology, and related publications and device development in single cell area are growing exponentially. The enthusiasm of single cell studies come from a basic knowledge that cells in a population behave differently and are unlikely to be identical (Schmid, Kortmann, Dittrich, & Blank, 2010). On the other hand, conventional cellular research is conducted by using bulk cells, and resultant data demonstrate only the averaged signal. The readout from studies at the bulk cell level is overly smoothed, and fails to explain how a subgroup of cells can survive against rapid environmental changes. However, cell-to-cell differences demonstrate mechanistic pathways for studying the benefits of heterogeneity (Avery, 2006). Furthermore, some fatal diseases develop from the single cell level, and phenotypic heterogeneity studies delineate the keys to pathogenesis and pathophysiology (Suresh et al., 2005). For example, at the beginning stage, the population of malignant tumor cells is very limited. However, rapid growth and accumulation will eventually damage normal tissues and the immune system (Loeb, 2003). Therefore, the detection of a single mutated cell could contribute significantly to the early diagnosis and treatment of cancer.

The morphology of a cell provides useful information for diagnosing disease. For example, the irregular nucleus in terms of size, shape, and internal distribution indicate cancer initiation and progression (Nandakumar, Kelbauskas,

R. Johnson, & D. Meldrum, 2011). In single cell studies, the nuclear morphology can be detected by using modern imaging devices and techniques. However, conventional optical microscopy for single cell studies is two-dimensional (2D) and does not represent the true three-dimensional (3D) structures of cells and their internal organelles (M. G. Meyer et al., 2009). This limitation inhibits the quantitative investigation of cellular morphological. With 2D imaging, contents inside of a cell overlap and are distorted. The quantity and volume of each component has to be estimated or guessed by users. The lack of information inside of a cell parallel to the illumination source may mislead the researcher. On the other hand, multiple-perspective microscopy successes stereographic cellular anatomy, and facilitates 3D image reconstruction. 3D single cell CT, as shown on Figure 2.1, is similar to x-ray computed tomography (CT). First, a cell is stained so that different parts have different absorption. A series of pseudoprojections are then taken by optical microscopy and a CCD camera, and the filtered backprojection reconstruction method is applied to return a 3D image that can then be compared to the knowledge bases of pathologists and cytologists (Fauver et al., 2005). Unlike regular CT, the imaging acquisition component for cellular study is fixed on a stage. Therefore, to enable multiple-perspective images, a cell must rotate around a fixed axis perpendicular to the viewing direction. However, rotating individual cells is challenging since it involves both trapping and rotation.

2.2 Existing techniques for single cell rotation

On the micro scale level, mechanical micromanipulation provides precise user control with multiple degrees of freedom for single cell operation, as demonstrated by bio-aligners, microrobotic arms, etc. (Jager, Inganäs, & Lundström, 2000)(Arai, Kawaji, Luangjarmekom, Fukuda, & Itoigawa, 2001). These micromanipulation methods use multiple micro actuators and micro robotics on very complex experimental platforms with high cost. Even worse, the mechanical methods require direct physical contact, and exert strong stimuli that may introduce physical and biological modifications (Lin, Lai, H. P. Liu, Chen, & Wo, 2008). Cells may also suffer from contamination and damage from physical contact. Currently, the commercial Cell CT system rotates cells within a capillary tube as shown in Figure 2.1. Cells are first fixed and then immobilized in a capillary tube with refractive index matching gels. They are then rotated around a fixed axis as the capillary tube rotates (Miao et al., 2009). However, the current cell rotation device has two major disadvantages. First, the rounded capillary tube introduces imaging distortion, and requires extra work to correct errors. Second, the refractive index matching gels are not biocompatible. As a result, only fixed cells can be used in this platform, and many important investigations, such as drug response over time and functional imaging, are impossible. To solve current problems, a new cell rotation method with a flat imaging surface and biocompatible environment must be proposed.

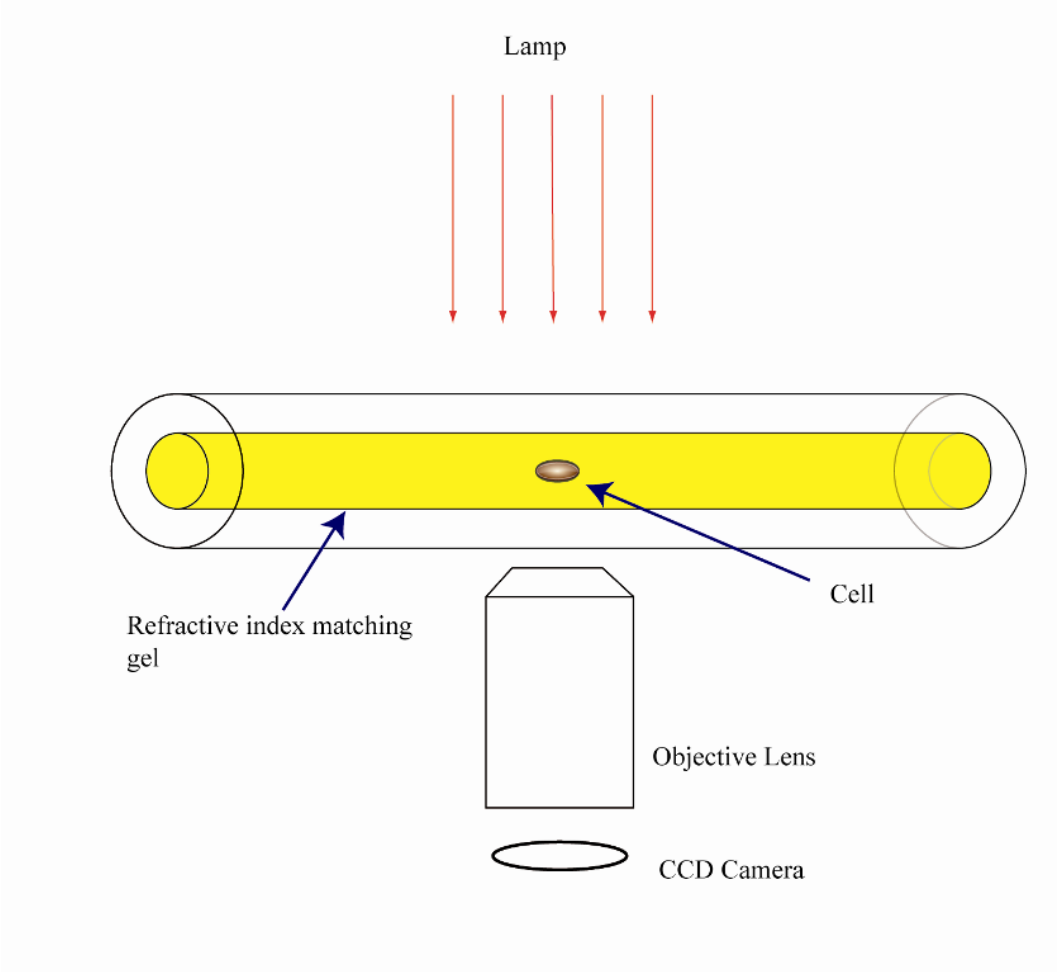

Figure 2.1. Schematic of the conventional Cell CT system

A more viable option is to use a microfluidic approach to manipulate and analyze single cells in real time within a controlled environment void of direct physical manipulator contact (Lidstrom & D. R. Meldrum, 2003). Microfluidic devices are well acknowledged tools for chemical, biochemical and biological studies since the surface-to-volume ratio is significantly increased and the laminar flows can be achieved in most cases (Eriksson et al., 2007). Microfluidic rotation mechanisms that use ultrasound, dielectrophoretic force, electric field, or Lorentz forces are well-studied (Yamakoshi & Noguchi, 1998)(Brehm-Stecher & E. A. Johnson, 2004) (Lin et al., 2008). However, these methods usually require

intricate equipment setups and call for extensive microfabrication processes to produce micro-actuators, micro-electrodes, etc. Shelby *et al*. introduced the use of hydrodynamic forces to rotate a cell with relatively simple microfabrication processes. This technique relies on a micro vortex that is formed within a side chamber attached to a long straight channel. Figure 2.2 shows the formation of this secondary recirculation inside of a diamond-shape side chamber. The microvortex generated from the flow detachment in the chamber enables the investigation of high radial acceleration and shear stress applied to the single cells (Shelby, D. S. W. Lim, Kuo, & D. T. Chiu, 2003)(D. Chiu, 2007)(Shelby & D. T. Chiu, 2004). However, it is believed that relatively high shear stress levels induce morphological and biological modification on cells (K. Liu et al., 2008). On the other hand, low shear stress in the less dynamic region of the side chamber provides an ideal environment for cellular nutrition with waste removal function (K. Liu et al., 2008)(Lin et al., 2008). The hydrodynamic rotation method represents an attractive cell manipulation option since it demonstrates the capability to transport and rotate a single cell, with precise control, while ensuring a favorable cellular environment.

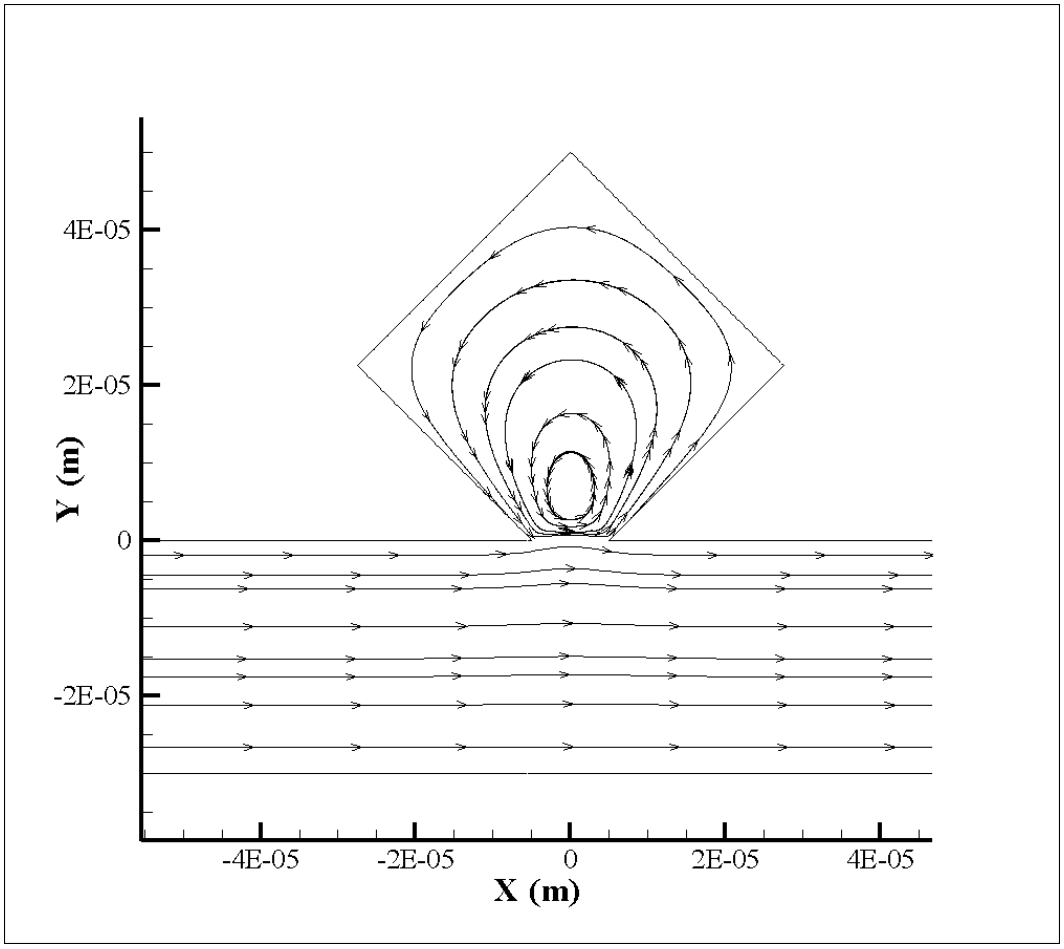

Figure 2.2. Simulation of the microvortex in a diamond-shape side chamber duplicated from the study of Shelby *et al*. Direction of the flow is presented by streamlines with arrows

2.3 Investigate flow profiles in microvortex systems

In order to rotate a single cell under a controlled and desirable manner, the fluidic velocity profile must be well understood. However, the flow profile inside of a microvortex system has not been completely quantified yet. Computational fluid dynamics (CFD) models have demonstrated the formation of flow recirculation inside of the chamber and the flow detachment between the chamber

and channel. CFD was previously used to evaluate and compare the design of the diamond and double diamond-shape side chambers (D. Chiu, 2007)(Shelby, Mutch, & D. T. Chiu, 2004). Bahk *et al*. applied CFD for developing a micro-centrifuge device with a rectangular side chamber (Ha, Bahk, et al., 2007). Unfortunately, CFD results are simulated under ideal conditions and are assumptive. In the real world, especially on the micro scale, flow may not behave in the same way as simulation. On the other hand, experimental methods encountered many challenges due to the extensive dynamic range of velocity in a small area of micro scale, which requires that experimental devices include both high resolution and accuracy. Shelby *et al*. built angular velocity profiles by tracking the change in backscattered laser light from an ablated polystyrene particle and the change in fluorescent signal from a single cell (Shelby et al., 2004). Flow tagging velocimetry (FTV) presents an alternative to characterize the flow profile (Shelby & D. T. Chiu, 2003). However, FTV requires a more complicated setup that includes an additional pulse laser to activate photoactivated fluorophore in the flow. Furthermore, it is incapable of sub-micron resolution. Mapping 2D flow profiles using FTV also requires additional automation and computational reconstruction techniques, since FTV only measures 1D velocity at any instant (Shelby & D. T. Chiu, 2003).

Applying micro particle-image velocimetry (μ-PIV) to investigate recirculating flow is a more suitable approach. Santiago et al. introduced the first μ-PIV systems to demonstrate slow motion flow with micro scale resolution (Santiago, Wereley, Meinhart, Beebe, & Adrian, 1998). Later the invention of

Nd:YAG lasers (New Wave, CA, USA) enabled the detection of high motion flow (meters/second) (*Particle Image Velocimetry a Practical Guide*, 2007). After that μ-PIV became a popular method for understanding detailed fluid motion inside of microfluidic channels, since it was too difficult for numerical simulation to adequately explain phenomena in many complex microfluidic (*Particle Image Velocimetry a Practical Guide*, 2007). One relevant study applied μ-PIV to investigate the microvortex produced by active microcentrifugation with electrodes (Qin, Yeo, & Friend, 2009). Later studies showed further progress in toward effective micro-PIV investigation of microvortices (Ha, Y. K. Bahk, et al., 2007). On the millimeter scales, Ota *et al.* applied two parallel counter flows to generate circulation, and the associated PIV work demonstrated rotational velocity profiles inside of the chamber (Ota et al., 2010). However, no experimental data describing fluid velocity profiles of microvortices in a side chamber have been presented.

2.4 System overview

The diamond-shape side chamber microvortex system is not compatible with multiple perspectives microscopy because it has a sharp corner toward the image acquisition surface, as shown in Figure 2.2. In this thesis work, a trapezoidal side chamber is developed to address the optical requirement. The proposed system is displayed in Figure 2.3. The system includes a main channel for letting liquid and cells pass through, and a side chamber for generating microvortices. A single cell can be trapped and moved into the chamber with optical trapping. The

recirculation flow formed in the chamber can then rotate the cell. Illumination is provided from the side of the channel, and the objective lens takes images from many angles while the cell rotates. Parameters including the interface angle (α), length, width, and height are indicated in Figure 2.3.

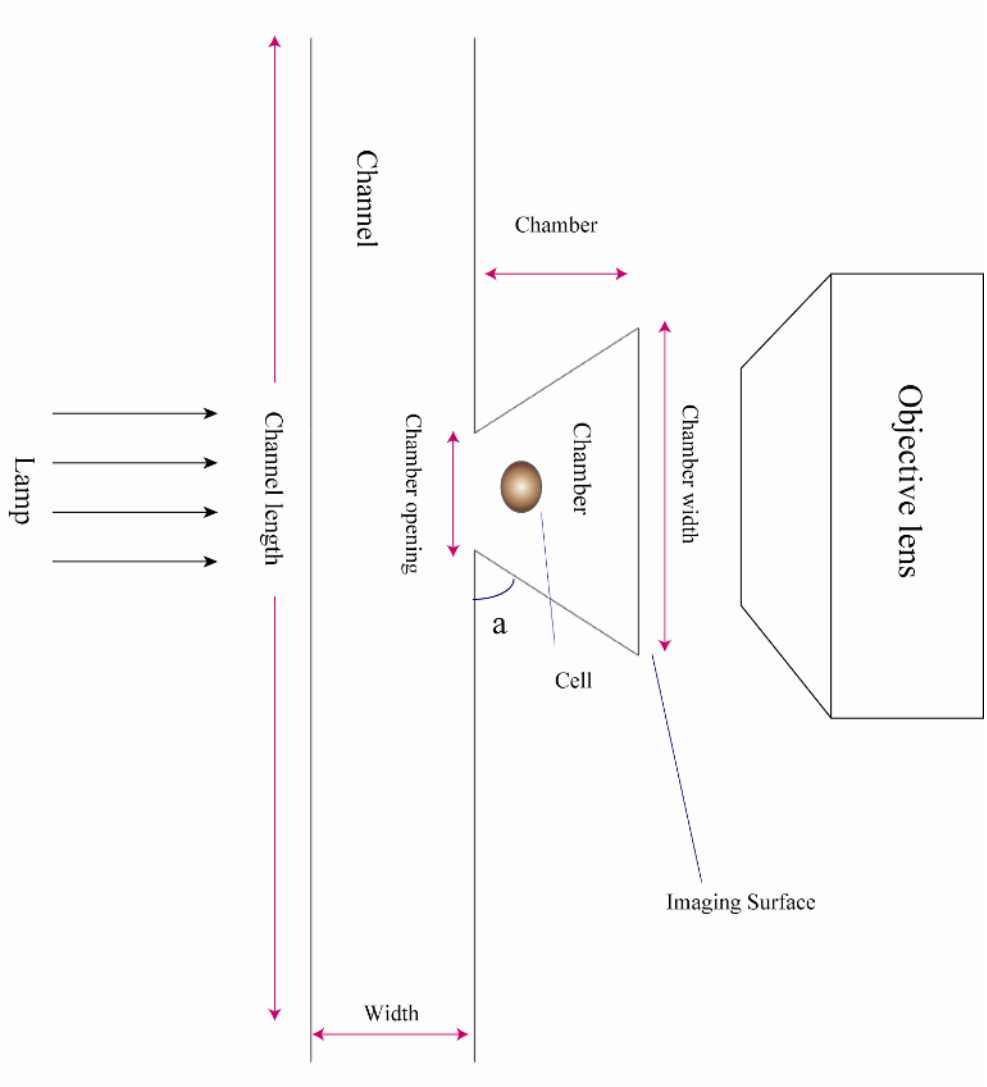

Figure 2.3. Overview of the proposed trapezoid side chamber system

Chapter 3

DESIGN THE SINGLE CELL ROTATION SIDE CHAMBER WITH COMPUTATIONAL FLUID DYNAMICS (CFD)

This project starts with numerical simulation with CFD, since the design of the side chamber is not too complex to challenge the ability and accuracy of the current existing CFD software. CFD has advantages of low cost and high efficiency. Experimental methods on micro scales rely on expensive microfabricated molds and devices, and the cost grows exponentially with quality. In the early development stage, knowledge of the desired geometry for side chambers and associated design parameters is limited. Therefore, numerical simulation eliminates high cost of molding. Furthermore, experimental methods usually require one week from fabrication to data processing with high possibilities of failures. However, a 2D simulation can be finished in a day after sufficient training. In this project, CFD provides the first step to optimize chamber geometry and design parameters including optical access.

3.1 Software and Mathematics

In this study, geometries and meshes were created using Gambit (ANSYS Inc, PA, USA). Computational fluid dynamics (CFD) models were applied by solving incompressible steady state Navier-Stokes equations. A finite volume method software Fluent 6.2 (ANSYS Inc, PA, USA) was used to construct a two-dimensional (2D) and three-dimension (3D) velocity profiles. The SIMPLE algorithm and a non-slip boundary were applied for the solver, and the material of flow was water.

In general, Fluent solves both mass and momentum conservation equation for laminar flow. Equation 3.1 (*Fundamentals of Momentum, Heat, and Mass Transfer*, 2001) demonstrates the mass conservation equation:

$$\frac{\partial \rho}{\partial t} + \nabla \cdot (\rho \vec{v}) = R, \tag{3.1}$$

where R is rate of mass produced into the system, $\vec{v}$ is the velocity vector and ρ is the density of the liquid. $\rho\vec{v}$ describes the flux in this system. In this study, no reaction occurs, and flow is incompressible. Therefore R=0, and $\frac{\partial \rho}{\partial t} = 0$. Equation 3.1 is simplified as:

$$\nabla \vec{v} = 0. \tag{3.2}$$

The momentum conservation equation is represented in Equation 3.3 (*Fundamentals of Momentum, Heat, and Mass Transfer*, 2001) as Navier-strokes format:

$$\rho \frac{\partial \mu}{\partial t} + \nabla P = \rho g + \mu \nabla^2 v, \tag{3.3}$$

where P is the pressure term, and μ is the dynamic viscosity.

3.2 Factors affecting microvortex formation

Previous studies conclude that the size of the chamber opening, surface roughness, chamber geometry, and flux are key factors associated with microvortex formation in the side chamber (D. Chiu, 2007). However, details must be revealed for a better understanding of the phenomena behind the formation of microvortex.

3.2.1 Size of the chamber opening

The size of the chamber opening is a critical parameter affecting the formation of a recirculation flow. After further investigation, I found out that the ratio β,

$$\beta = \frac{Chamber\ opening}{channel\ width}, \tag{3.4}$$

was a more specific key factor. In this study, I simulated several square-shape side chambers with the same channel width but different chamber openings. To ensure simulations were under a controlled condition, the same inlet velocity (0.02cm/s) and meshing protocols were applied. Geometry and meshing were demonstrated in Figure 3.1. (A) - (D) displayed four square chambers with different openings at the interface between main channel and side chamber. The main channel was 1.6 mm in length and 30 μm in width. The side chamber was a square with 40 μm side length. Each individual case was constructed with 20500 structured quadrilateral elements. As described in Figure 3.1(D), the meshes

within the chamber had higher density than in main channel to ensure greater resolution of simulation readouts in the area of interest.

Figure 3.1 (A) - (D) shows streamlines generated from different systems. The ratios β of chamber opening to the channel width were 4/3(A), 1(B), 0.5(C) and 0.25(D). It is clear that the flow in Figure 3.1 (A) does not detach at the interface between the chamber and channel, so the recirculation flow is not formed at the center of the chamber. In Figure 3.1 (B) the counterclockwise recirculation forms inside of the chamber. However, the shape of vortex is irregular instead of circular. On the other hand, circular shape recirculation streamlines are demonstrated inside of square chamber in Figure 3.1 (C) and (D). This result suggests that a small chamber opening to channel width is required to form a microvortex in a side chamber. Furthermore, the smaller the ratio, the more circular the vortex will be.

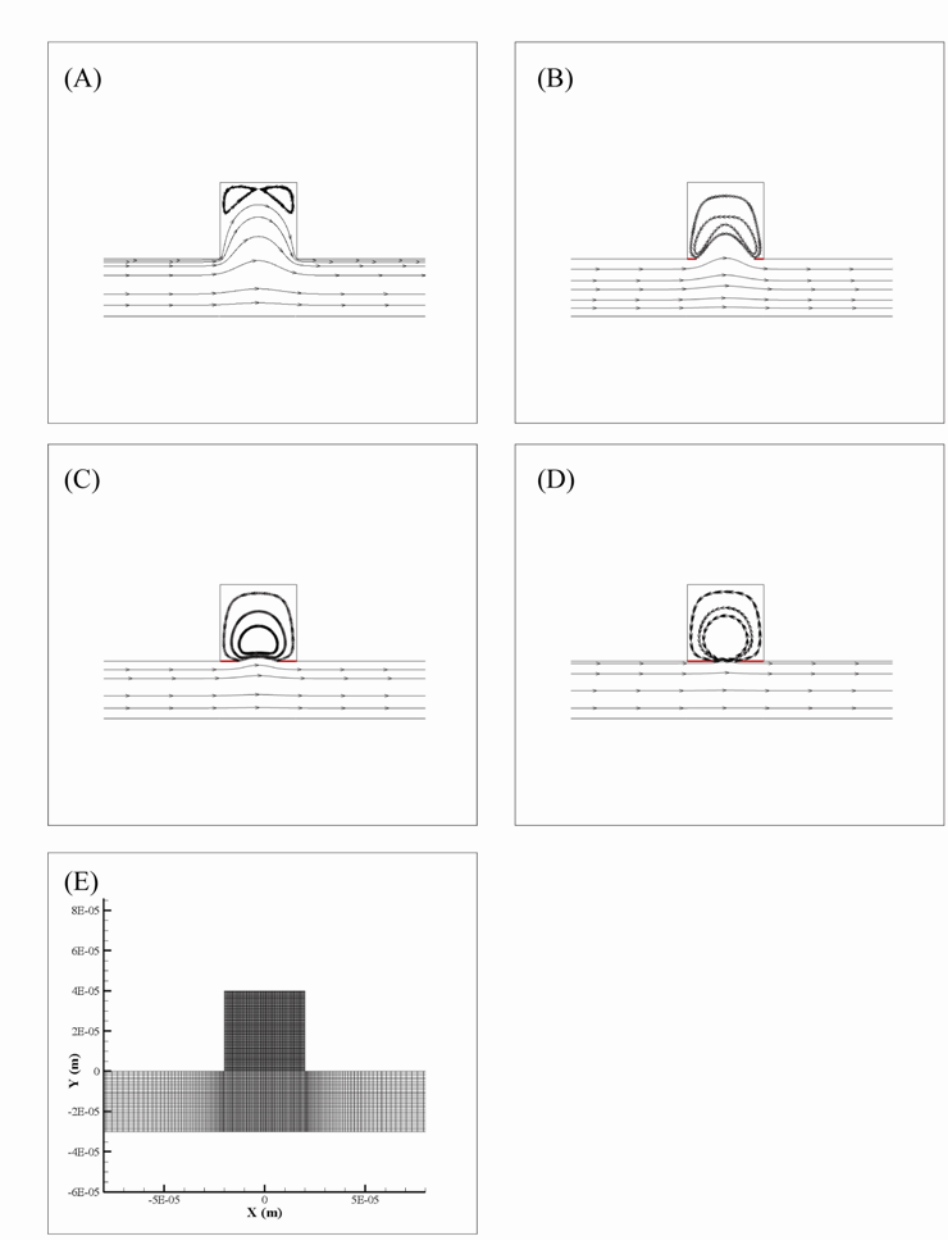

Figure 3.1. Simulation of square chambers with different openings. (A) 40 μm chamber opening; (B) 30 μm chamber opening; (C) 20 μm chamber opening; (D) 10 μm chamber opening; (E) Geometry and meshing

3.2.2 Inlet Velocity

Inlet velocity is the only parameter that can be controlled by users during actual experiments. It is believed that the strength of the vortex is controlled by the inlet velocity. In this study, I investigated the correlation between inlet velocity and the microvortex property.

The simulation was based on a diamond-shape model, since it is being heavily studied in previous work and is known as a geometry that produces stable microvortices. In our simulation, inlet velocity varied from 0.01 μm/s to 1 m/s. For each simulation, the vorticity value at the vortex center was measured. A linear regression model was created to fit the vorticity of the vortex center with inlet velocity in Figure 3.2. In the real world, monitoring and controlling the vorticity in a microvortex system are is difficult, because there is no easy measurement device for detecting rotation rates very quickly. Therefore, it is extremely useful to find an appropriate inlet velocity at the beginning of experiments. For example, if a user wants to achieve a desired vorticity at the vortex center for a specific engineering requirement, this linear model can be easily applied to design the inlet velocity.

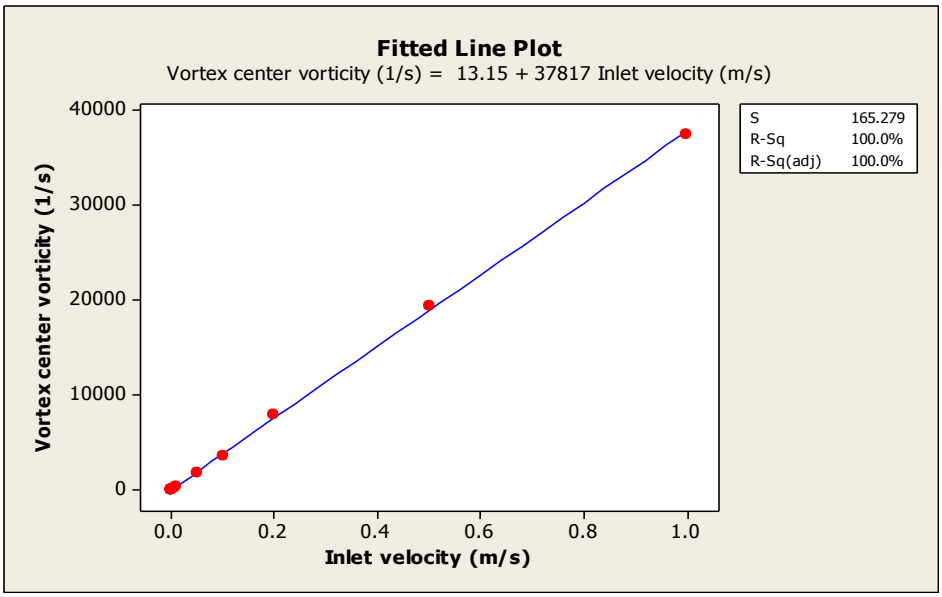

Figure 3.2. Linear regression fitting of vorticity vs. inlet velocity. In this figure, a linear relationship between inlet velocity and vortex center velocity is demonstrated . The R^2 value is 99.9%.

3.3 Side chamber with different geometries

3.3.1 Method

A rectangle-shape, isosceles trapezoid-shape, and diamond-shape side chambers, each attached to a long straight channel, were investigated. The main channels were designed as 700 μm in length and 50 μm in width. Structured quadrilateral elements were applied to mesh the main flow channel with 5125 elements. The opening between each channel and chamber was 40 μm. Trapezoid-shape and rectangle-shape side chambers had the same height (60 μm), and the diamond-shape side chamber had a height of 130 μm. The longer parallel side of the trapezoid-shape side chamber was 140 μm, while the lower half of the diamond-shape side chamber was identical to the trapezoid-shape chamber. Since the microvortex would occur within the side chamber, the density of nodes on the sides of this cavity was set to 1 μm/node to insure high. Structured quad meshes were applied for the rectangle-shape side chamber, which resulted in 2400 quadrilateral elements. On the other hand, a combination of unstructured quadrilateral and triangular meshing was applied for the diamond-shape and trapezoid-shape side chambers. The diamond chamber generated 10151 elements, while the trapezoid one generated 5360 elements. The detailed geometries and meshes are described in Figure 3.3.

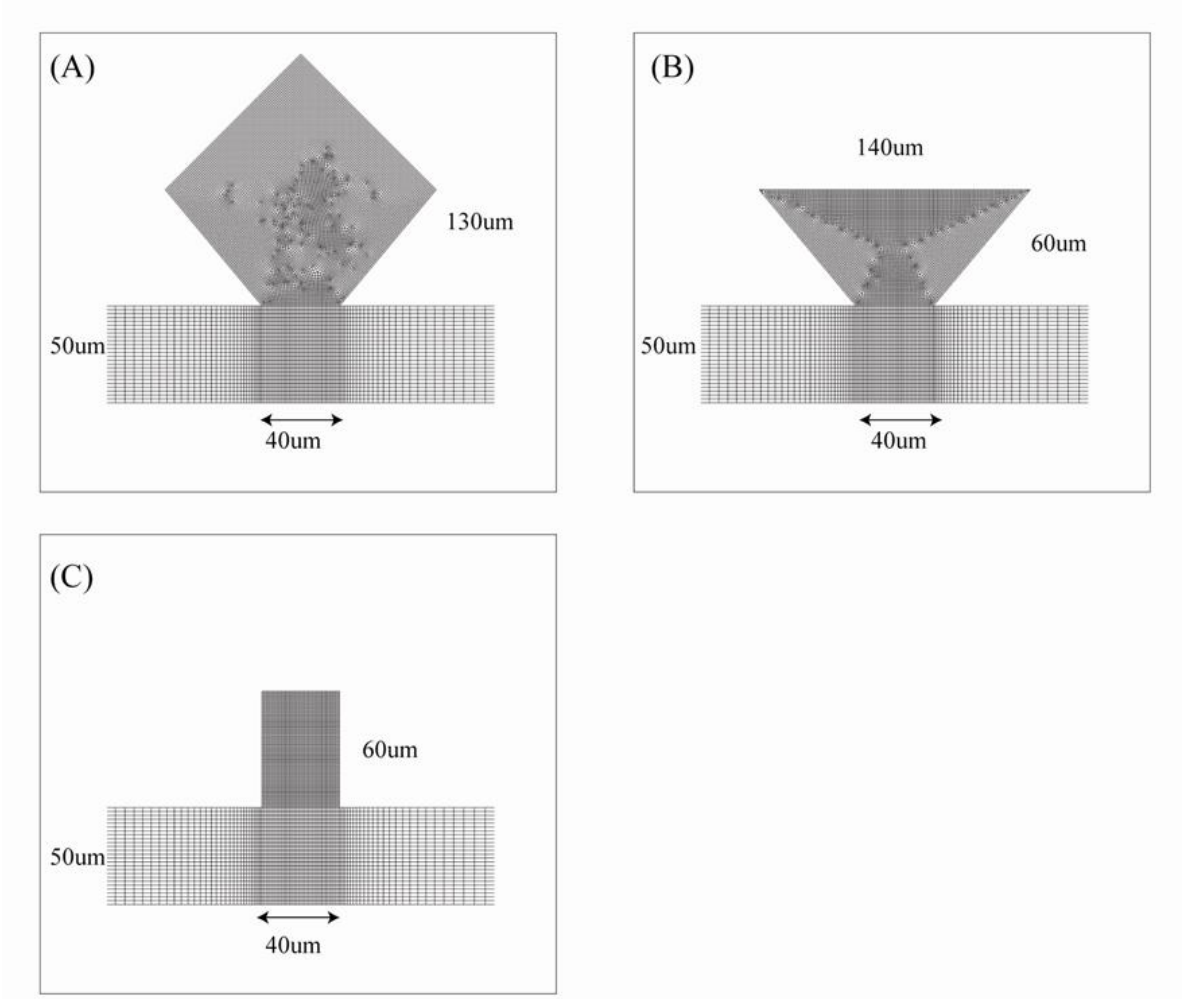

Figure 3.3. Geometry and meshing of three different side chamber designs: (A) diamond-shape side chamber; (B) trapezoid-shape side chamber; (C) rectangle-shape side chamber

3.3.2 Evaluation for final design

To assist chamber designs, three different geometries of side micro-chambers were simulated and performance was compared. The streamtraces (streamlines) generated with an inlet velocity of 20 μm/s are shown in Figure 3.4. The ratio of chamber opening to channel height is 0.8 for all three cases. Case (A) and (B) share the same steepness of the lower sides, and Case (B) has the same chamber height as (C). The flow direction in the main channel for all three geometries is from left to right, and the circulation of flow in side chambers is in a counterclockwise direction. Flow detachments from the channels into the side chambers and microvortices within the chambers were apparent in paths of streamlines.

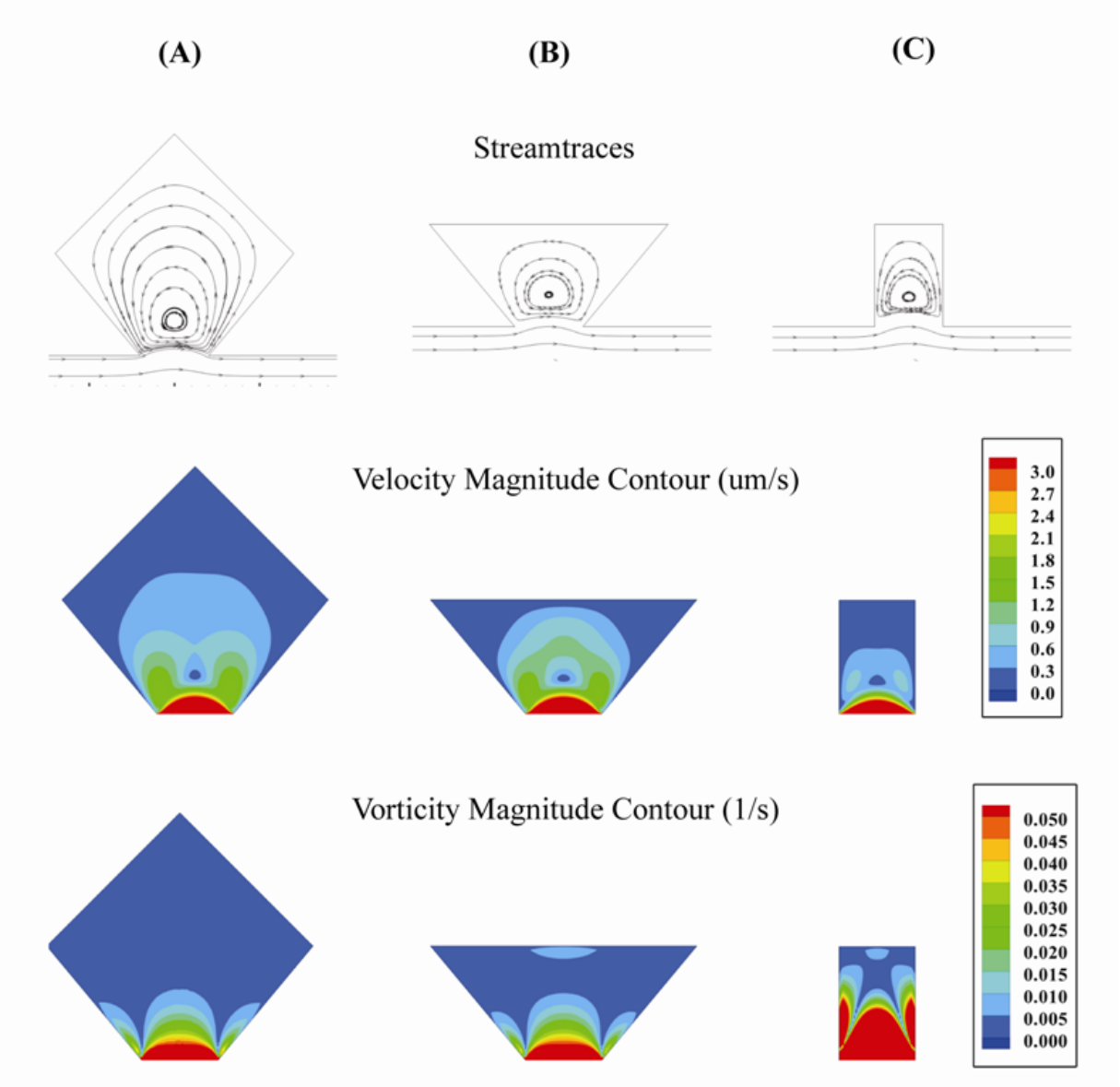

Figure 3.4. CFD simulation of three different chamber designs in columns: Diamond (A), Trapezoid (B), and Rectangle (C). The first row demonstrates the streamlines, the second row demonstrates the velocity magnitude contour, and the third row demonstrates the vorticity magnitude contour

Figure 3.5 compares the position of vortex and the total circulation among three designs. The position of the vortex center (Figure 3.5A) is an essential parameter, since displacement from the flow channel can prevent a cell from being dragged into the faster main flow. Furthermore, the side imaging microscope lens has very limited working distance, so displacement from main channel also improves optical imaging quality and accessibility. The trapezoid and diamond chambers displaced the vortex center 6.3% and15% away from the flow channel as compared to the rectangular chamber (Figure 3.3A). Total circulation (Figure 3.3B) demonstrates the strength of the vortex, and it is related to the size of the chamber. The Trapezoidal chamber achieves 61% more circulation than the rectangular one. However, the difference between the trapezoid and diamond chambers in total circulation is only 6.6%, which does not represent a significant difference.

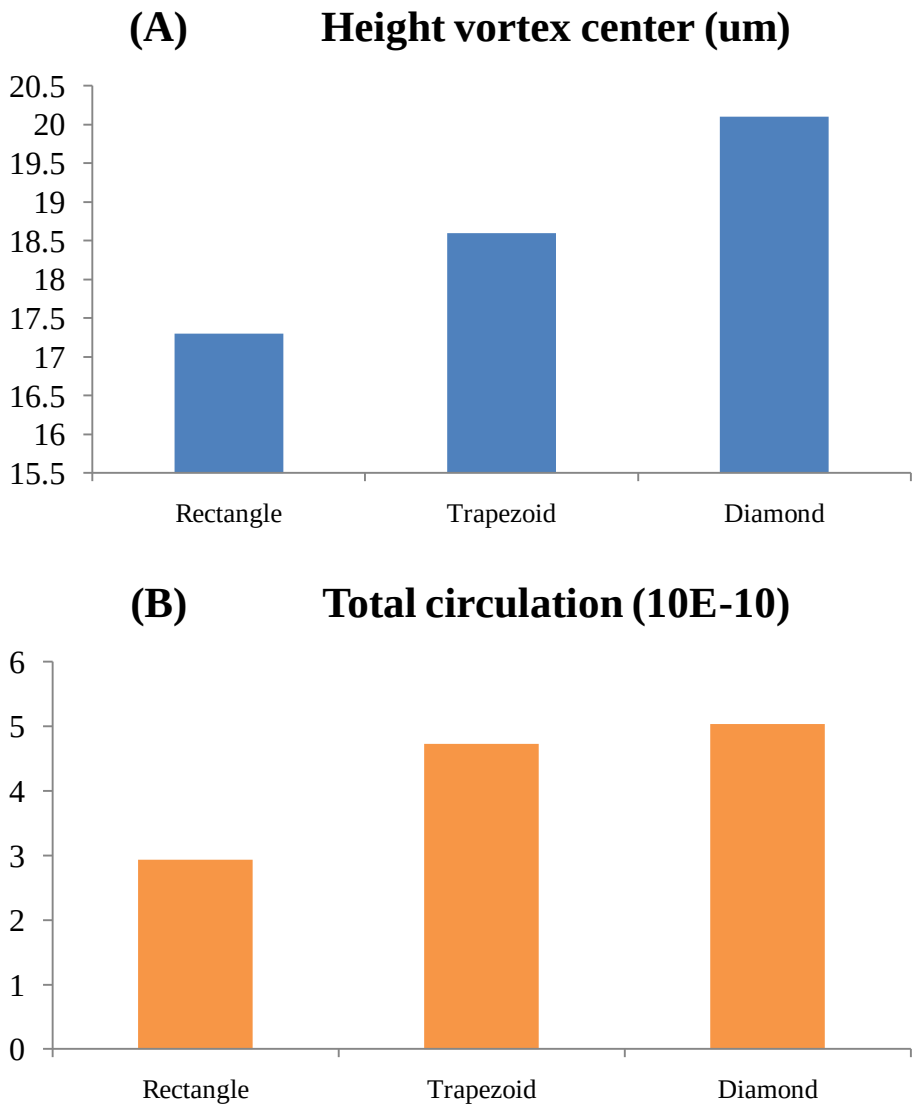

Figure 3.5. Comparison of vortex center location (A) and total circulation (B) among three different chambers

In order to achieve the goal of multiple-perspective imaging by using brightness field illumination, a flat side plane which is parallel to the main channel is desirable. Among the proposed designs, the diamond-shaped side chamber with a corner at the imaging surface, which has been extensively studied

by Chiu's group, does not provide imaging accessibility, so it is omitted from consideration. The rectangular and trapezoidal side chambers provide excellent optical access. In order to form a microvortex, a small chamber opening to channel width ratio is required as discussed in 3.2.1. However, with the same chamber opening size, the trapezoid-shape chamber offers larger side imaging plane. Furthermore, the trapezoid-shape chamber provides better total volume than the rectangular-shape chamber, and this benefit will improve the quality of PIV experiments significantly by allowing more tracing particles to enter the chamber. The streamline graph in Figure 3.4 demonstrates that the shape of the streamlines in the rectangular chamber is more narrowed than in the trapezoidal chamber. On the other hand, the trapezoidal chamber shows well expanded circular streamlines. Vorticity contours in Figure 3.4 indicate that the vortex center in rectangular-shape chamber is located at a point surrounded by maximum vorticity, which may harm the stability of the system. The difference in performance between trapezoid-shape chamber and rectangle-shape chamber is caused by the expanded lateral parts. With some chamber expansion in the lateral direction in a smaller interface angle, the separated flow is able form smoother recirculation in the trapezoidal chamber. Accordingly, the trapezoidal chamber was selected as the best design.

3.4 Optimizing design parameters

There are two primary aspects of engineering requirements associated with optimization. One is the microfabrication requirement, and the other is the optical access requirement. The difficulty of microfabrication depends on the complexity of the geometry. In this study, the angles of corners are the main challenges for high resolution microfabrication. The imaging acquisition microscope has very limited working distance, so a chamber with smaller height is favorable.

3.4.1 Influence of the interface angle

Interface angle (α) was the angle between the chamber and channel, as described in Figure 2.3. The above simulations of trapezoidal and rectangular side chambers demonstrate that the recirculation formed in the inner cavity is smoother for the geometry with an interface angle less than 1.57. In this part, I want to investigate the influence of the interface angle (α) further in a trapezoid-shape side chamber.

Three chambers with different interface angles were simulated (Figure 3.6). The main channel was 800 μm in length and 50 μm in width. Each chamber had 20 μm chamber opening and 30 μm chamber height. The only difference among them was the interface angle. Only the cases with interface angle less than 1 radian were discussed since they provide large imaging surface. In Figure 3.6, the interface angle of case (A) was 0.64 radians, case (B) was 0.40 radians and case (C) was 0.32 radians. Simulations were completed with an inlet velocity of 0.2 mm/s.

In Figure 3.6, I observed that the shapes of the recirculation flows for the three different cases were very similar. The only difference was the formation of secondary microvortices. Smaller interface angles tend to generate more minor recirculations at the two upper corners. The height of the vortex center was also measured and compared. Results showed that there was the height of the vortex center increased slightly with increased interface angle. However, the percentage of increase was less than 5%. Therefore, changing the interface angle did not impact vortex center position significantly. The vorticity at the vortex center was also compared, and the same result was found.

One limitation of this study is that only three simulations are investigated. Therefore, these results are only robust for the interface angle from 0.32 to 0.64. Beyond 0.64, the parameter associated with the vortex center might be more sensitive to the interface angle. For example, in section 3.3, the rectangular chamber has an interface angle of 1.57, and the interface angle of the trapezoidal chamber is 0.88. The differences between a 0.88 chamber and a 1.57 chamber are significant. However, the cost of microfabrication increases dramatically with the decrease of interface angle. Furthermore, the quality also fails to maintain robust with smaller interface angle. For example, sharp corners become rounded and surface roughness increases. In order to address the engineering requirement of microfabrication, a trapezoidal chamber with an interface angle about 1 was selected.

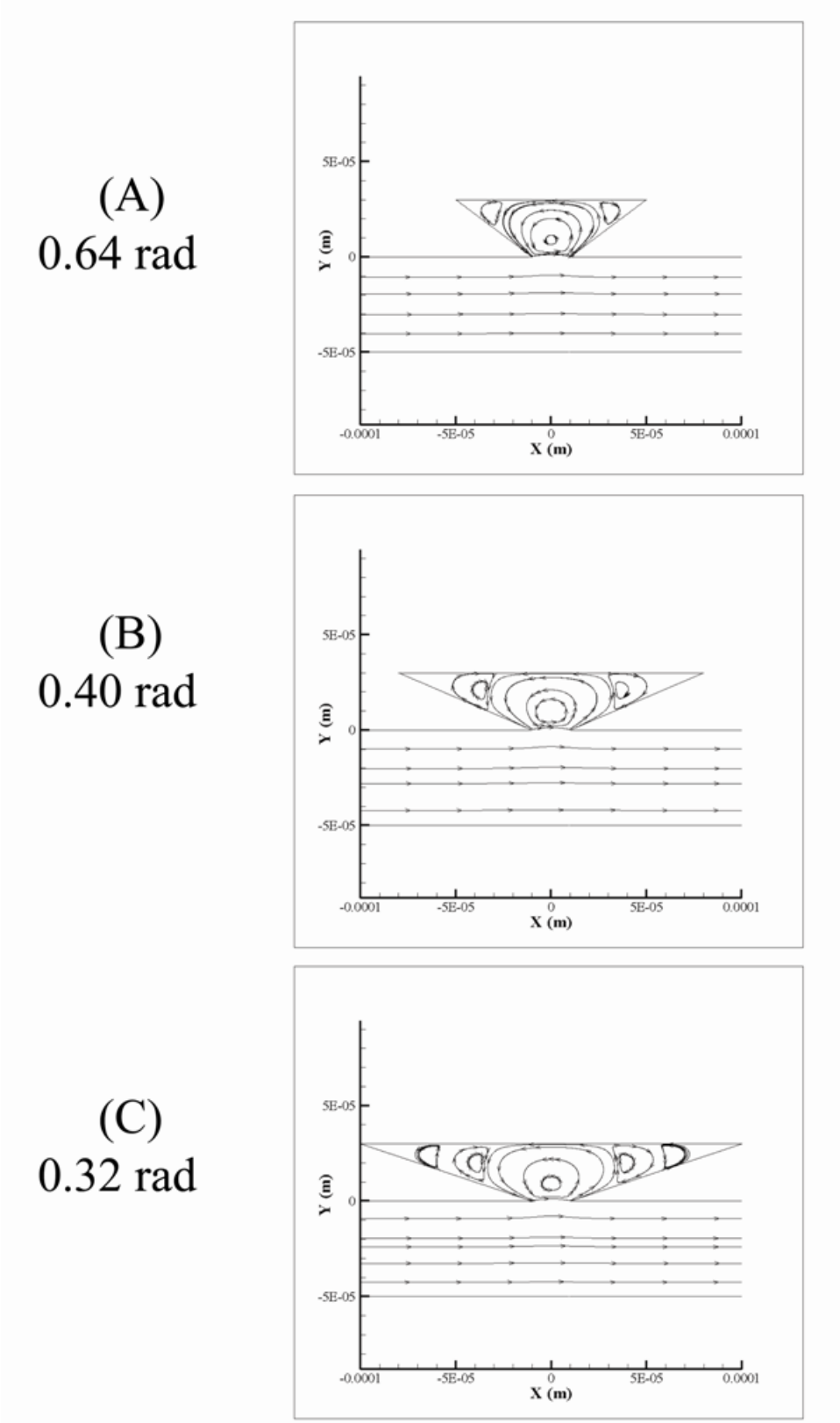

Figure 3.6. Influence of different interface angle on trapezoidal side chambers

3.4.2 Influence of the chamber height

The proposed imaging acquisition device includes a microscope lens with 100x magnification. However the 100x microscope lens working distance is very limited, ranged from 40 to 130 μm depends on types and manufactures. As a result, a chamber with smaller chamber can address this engineering requirement better. However, the influence of the added height on the trapezoidal chamber is unclear.

Four chambers with different heights were studied. In Figure 3.7, case (A) was the chamber with 10 μm height, (B) was the one with 25 μm height, (C) was the one with 30 μm height, and (D) was the one with 40 μm height. The main channel was 800 μm in length and 30 μm in width. All cases were simulated with 0.2 mm/s inlet velocity.

As shown in Figure 3.7, a secondary microvortex formed with the added height (Case D). However, the secondary microvortex was located at the region with extremely low velocity, which was considered near static. As a result, the influence of this secondary microvortex was negligible. The shapes of streamlines and velocity contours were very similar among B, C and D. Case A showed a more narrowed vortex than others. However, the height of the vortex center did not change significantly with increased chamber height. The same result also occurred in terms of the vortex center vorticity magnitude and the distribution of velocity. This concluded that the change in chamber height did not affect the overall flow behavior significantly. After further investigation, to qualify the

above conclusion, the minimum height of the side chamber must be larger than the chamber opening.

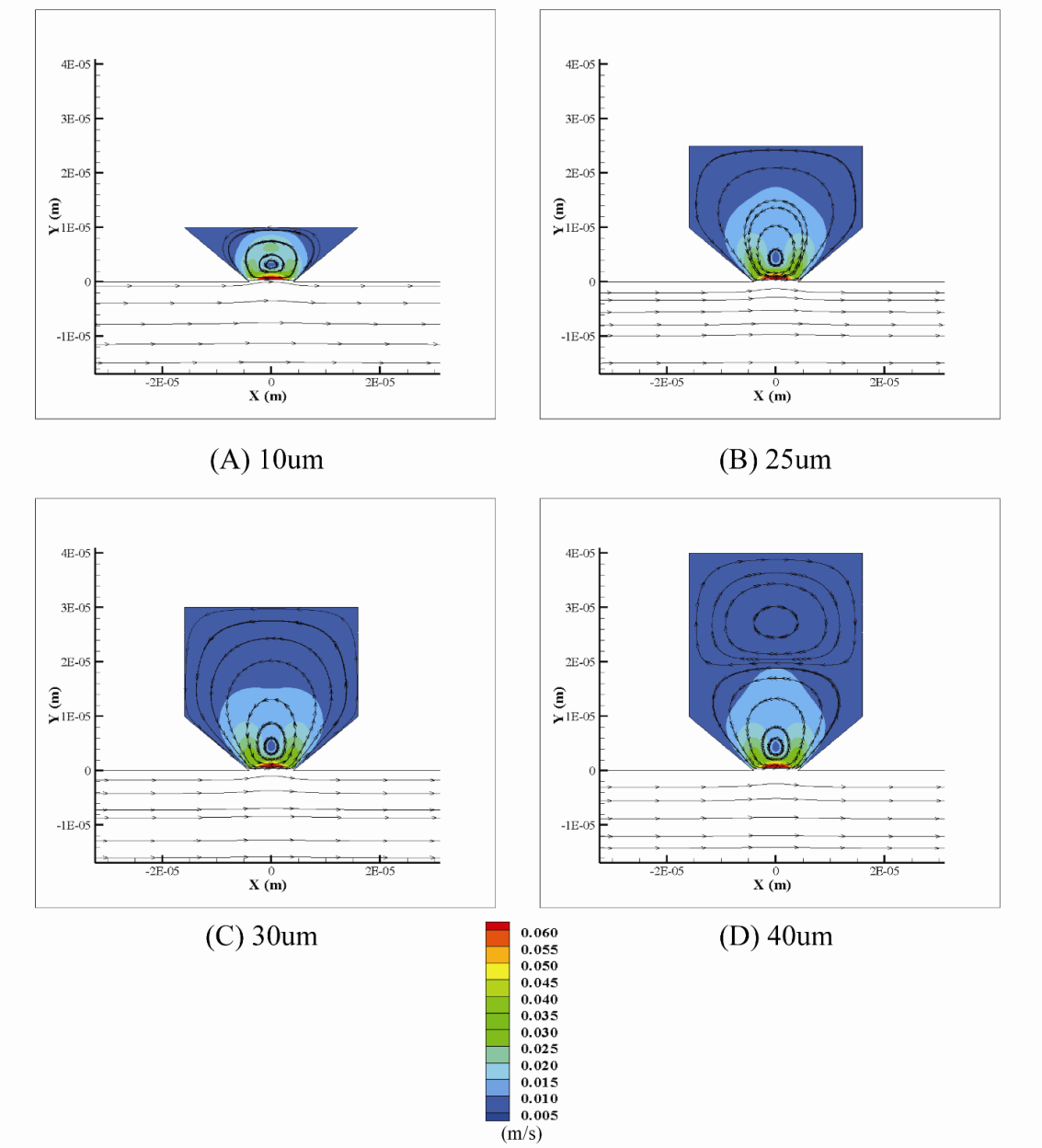

Figure 3.7. Side chambers with different chamber heights

Chapter 4

EXPERIMENTAL VERIFICATION WITH MICRO PARTICLE IMAGE VELOCIMETRY

4.1 Principle of μ-PIV

A μ-PIV system includes the following hardware as shown in Figure 4.1: inverted microscope, synchronizer, CCD camera, Nd: YAG laser and PC. An inverted microscope is the main platform of μ-PIV, and it enables sub-micron scale spatial resolution. The synchronizer is the core of this system and connects the PC, CCD camera and laser together with internal control, which allows the user to control the laser pulse delay, exposure time, laser trigger frequency, and time delay between two imaging frames through PC software. The charge coupled device (CCD) is capable of taking large amounts of recordings in one second, which allows the μ-PIV system to deal with different flow conditions. The Nd: YAG laser provides a high energy laser beam to excite fluorescent tracer particles. The PC provides general data acquisition, storage and processing capacities.

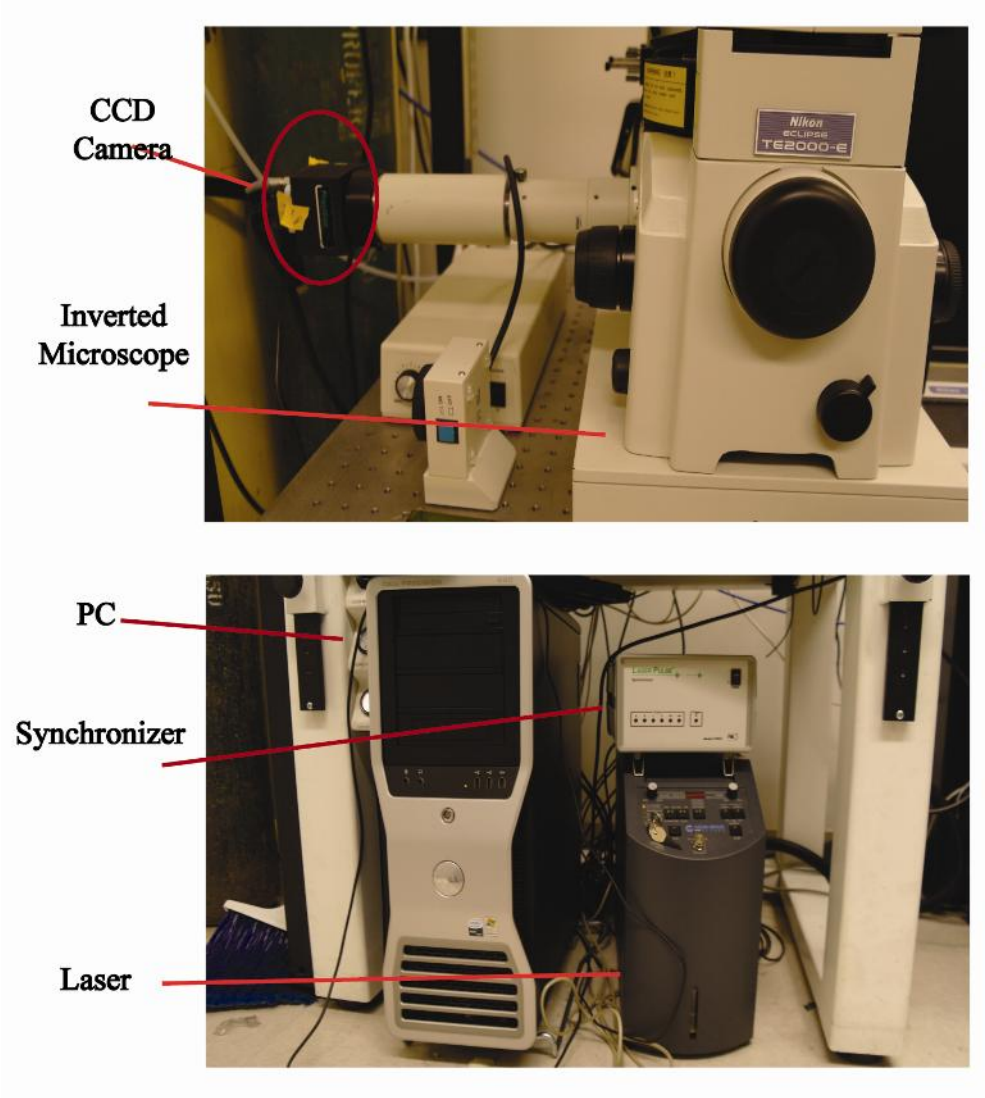

Figure 4.1. Hardware configuration of a 2D μ-PIV system

The data processing of the μ-PIV system is based on interrogation windows, which divide a PIV recording into many small subareas. Then, the displacement of particles between two frames is evaluated in each interrogation window by cross-correlation (*Particle Image Velocimetry a Practical Guide*, 2007).

4.2 Methods

4.2.1 Microfabrication

Since only the trapezoid-shape side chamber is considered as a viable design after comparing simulation results, the microfluidic device presented in Figure 4.2 was fabricated in polydimethylsiloxane (PDMS) with standard soft lithography methods using a 60-μm-thick KMPR mold.

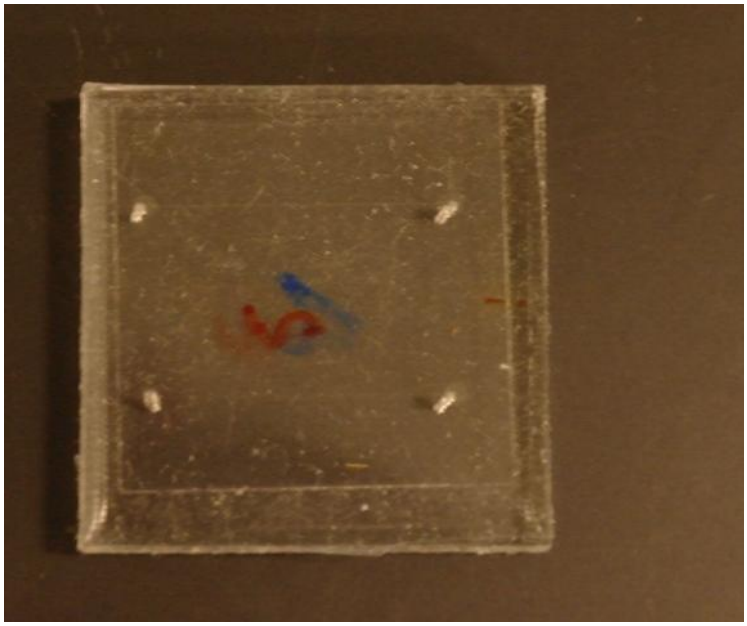

Figure 4.2. The microfluidic device made from PDMS

The rapid prototyping process is summarized as follows. First, monomers and cross-links were mixed with 10:1 ratio. Second, after mixing with glass rod, the mixture was degassed in a vacuum chamber for at least 30 minutes until all air bubbles disappeared. Then, PDMS were poured into the SU-8 mold and cured overnight. After curing, inlet and outlet holes were created by punching with an 18-gage stainless steel tube. PDMS chips and cover glasses were treated by a plasma cleaner (PDC-32G, Harrick Plasma, Ithaca, NY) for 40 seconds. This

process changed the affinity of the surface of both PDMS and cover glasses from hydrophobic to hydrophilic. After attaching the treated surface together, the PDMS layer was permanently bonded to the microscope cover glass. The dimensions of the main channel and the trapezoid-shape side chamber are shown in Figure 4.3.

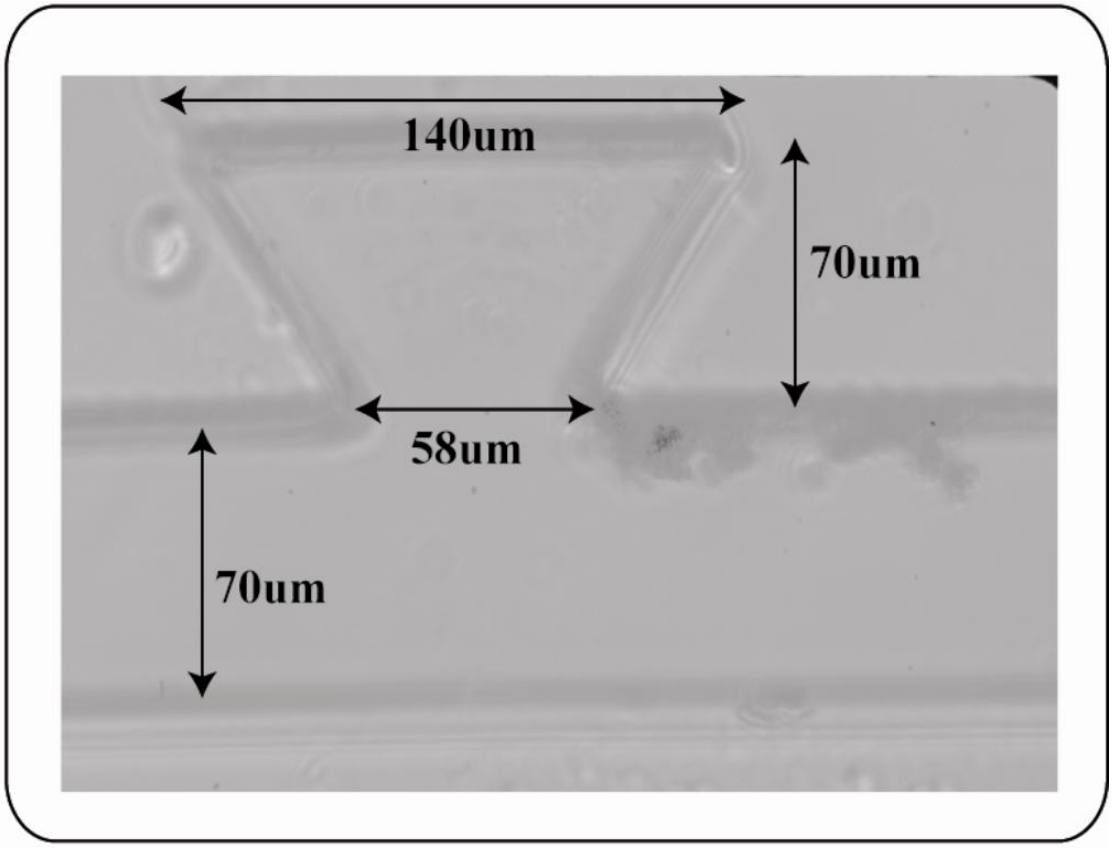

Figure 4.3. Dimension of the main channel and trapezoid-shape side chamber

4.2.2 μ-PIV experimental setup

A volumetric flow rate of 1 μL/s was supplied by a gear pump (milliGAT, GlobalFIA, WA, USA). Fluorescent particles of 1 μm in diameter (PSL,TSI, MN, USA) were diluted 10 times, and used for seeding. A 2D μ-PIV system (Micro-PIV, TSI, MN, USA) was applied to take a series of consecutive images within

the flow field. A schematic of the experimental setup is shown in Figure 4.4. This μ-PIV system was based on an inverted microscope (Eclipse Lv100, Nikon, Tokyo, Japan) platform. The microfluidic device was placed face down toward the objective lens of the inverted microscope. A CCD camera (Powerview Plus, TSI, MN, USA) was used to capture images at a resolution of 1600 x 1200 pixels. The illumination and excitation source was a Solo Nd:YAG laser (532nm, New Wave, CA, USA).

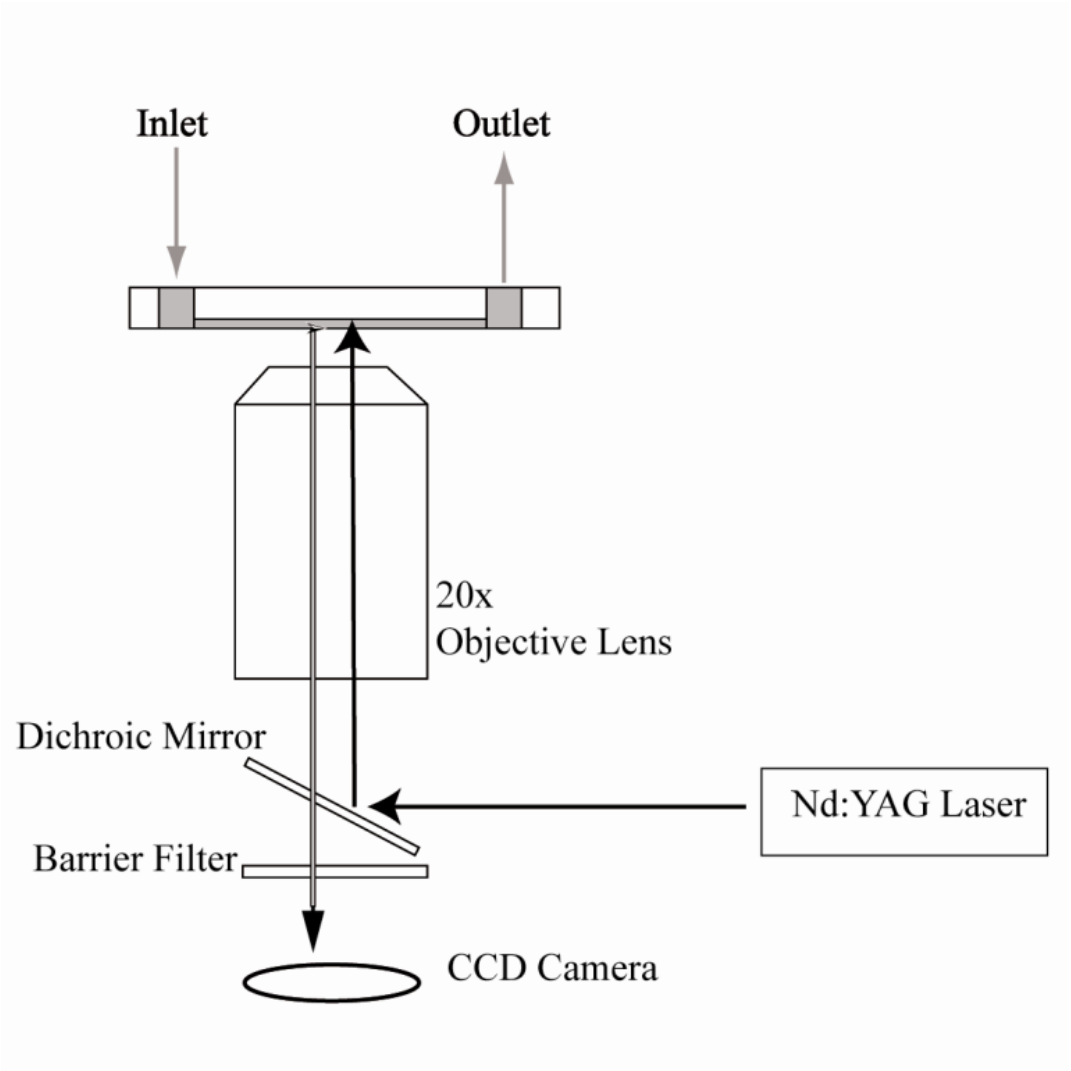

Figure 4.4. The schematic of the experimental setup and mechanisms

A filter cube containing a dichroic mirror filter and a barrier filter was integrated with the inverted microscope. The light path in the system is described in Figure 4.4. The laser wavelength of 532nm is reflected by the dichroic mirror to the microfluidic device. Then only the excited Fluorescent emission with wavelengths of 560 nm and above (>80% efficiency) can pass through the dichroic mirror. The barrier filter was used to block the light at laser wavelength to prevent it from reaching the camera or eyepiece because the high energy from the laser beam might burn CCD components or damage eyes. Emitted fluorescent particle signals are demonstrated in Figure 4.5. The brighter spots are the focused fluorescent tracing particles. The dimmer spots are the unfocused particles. The bulky fog located at the lower right corner of the trapezoid-shape side chamber was caused by the aggregation of tracing particles.

Figure 4.5. The emitted fluorescent signals in a sample frame

For the optical components, a 20x objective lens (NA=0.45) with a 2x camera projection lens produced a total magnification of 40x. With 40x total magnification, the entire trapezoid-shaped side chamber can be seen within the field of view. The u-PIV calibration parameter of 0.18 μm/pixel was calculated by using 0.30 mm x 0.22 mm field of view to divide the resolution. The focal plane was adjusted to the central plane of the microfluidic device. Two factors lead us to focus on the central plane instead of others. First, the PIV particle density is maximized in this plane, and in other planes there is no sufficient particle density to fulfill minimum particle requirement for each interrogation. Second, it is

believed that the PIV particles can suffer from wall-effect-induced lift force near the boundary, which makes the particles lag behind the flow (Park, Song, & Jung, 2009). The central plane is not as affected by the wall lift force.

4.2.3 Data acquisition and processing

In order to ensure that most particle displacements between two frames ranged from 1 to 10 pixels, a set of 400 image pairs was captured with a time separation between two images in a pair of 70 μs. The captured raw images were then processed using an ensemble cross-correlation algorithm by DaVis software (LaVision, Ypsilanti, MI, USA). Background noise was removed by subtracting the mean intensity of 400 image pairs. The trapezoid-shape side chamber region was the region of interest, so a mask with the same shape was applied to exclude everything else. A Gaussian weight function was applied to each interrogation window, which enhances the center of each particle to make it sharper. The averaged velocity vectors were obtained by applying a multi-pass recursive cross-correlation algorithm with 50% grid overlap. In this study, the initial interrogation window was set to 64 x 64 pixels, and the final was set to 32 x 32 pixels.

4.3 Comparison between CFD and μ-PIV

Velocity and vorticity magnitude contours from simulated and μ-PIV experimentation data for the trapezoid chamber are shown in Figure 4.5. For an inlet flow rate of 1 μL/s in the positive *x* direction, microvorticies can be observed in both (A) experimental and (B) CFD data. The velocity fields describe a counter-clockwise rotation inside of the chambers for both cases. The velocity magnitude contour plots of both (A) and (B) demonstrate a series of ring patterns.

The vortex center is the point in the circulation where velocity is zero, within the deep blue low velocity region at the center of the ring patterns. Comparing between (A) and (B), the vorticity distribution, the position of vortex center, and the velocity distribution are very similar. There is another small deep blue region at the lower right corner of the trapezoid-shape chamber in Figure 4.5 (A) due to its exclusion from the μ-PIV mask, because some particle aggregation occurs near that corner.

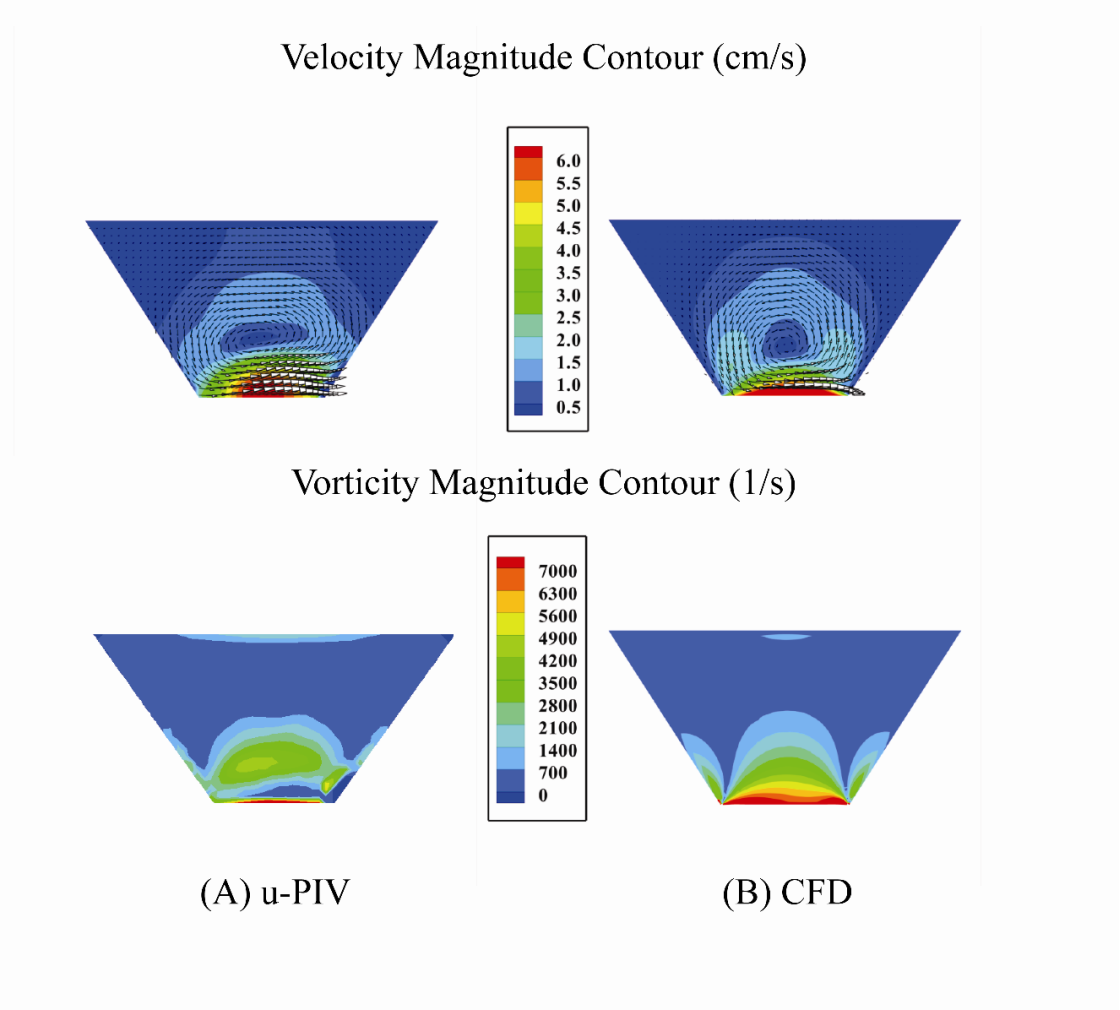

Figure 4.5. Velocity and vorticity magnitude contours for experimental (A) and simulation (B) results

The velocity magnitude surface plot for both μ-PIV experimental data (A) and simulated data (B) are shown in Figure 4.6. The meshing of this plot reveals the resolution, and it is clear that the CFD results have a higher resolution. The interrogation windows for μ-PIV were selected as 64x64 for the initial pass and 32x32 pixels for the final pass with 50% overlapping. The size of the first interrogation was chosen as 64x64 pixels because measurement error was significantly increased (based on root mean square errors (RMSE)) above 64x64 pixels. On the other hand, below 64x64 pixels, the high velocity regions were not measured well since the upper limit detectability of PIV is half of the first interrogation window. The overall shapes of the two plots are similar. CFD data shows higher magnitude at the channel-chamber interface than μ-PIV. This is reasonable since the velocity magnitude at the channel-chamber interface is very high, which exceeds the maximal detectable pixel displacements of μ-PIV setup (32 pixels).

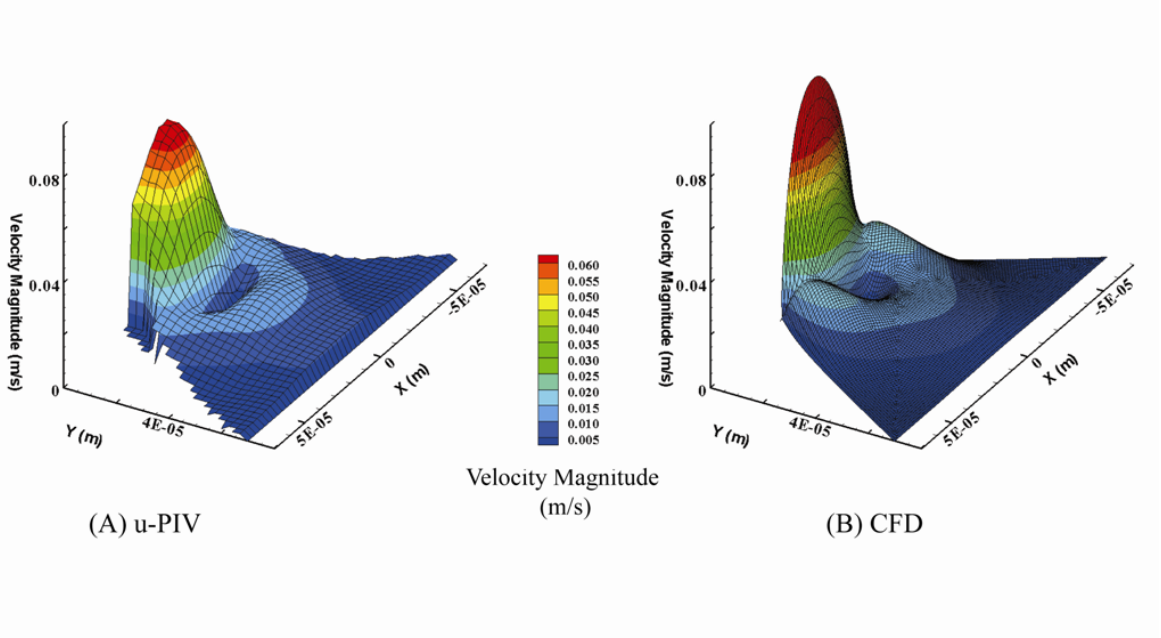

Figure 4.6. Velocity magnitude surface plots for experimental (A) and simulation (B) results

Outliers often present near the boundary areas of μ-PIV acquisitions. In this work, the vortex center area and the area far away from main flow show sub-pixel movement. On the other hand, the area near the interface between the channel and chamber demonstrates extreme pixel movement (>30 pixels), which is above the detectability of the interrogation window of the PIV algorithm in this study. Since the interest of this study is the formation of microvortex, Tradeoff was made that reduced the accuracy of the small area near the main flow. In order to compare the PIV experiment result with CFD quantitatively, statistical analysis is necessary. However, the velocity magnitude in the trapezoid chamber is not normally distributed. The nonparametric method does not require the normality prerequisite, so it is introduced in this work with the additional advantage of being robust to outliers. Specifically, the medians and variations of velocity magnitudes

are of interest. The Kolomogorov-Smirnov two-sample test is applied to test the null hypothesis that PIV and CFD results are identical with respect to location and dispersion. According to the μ-PIV vector density (2.88 μm/node), CFD resolution is smoothed to the μ-PIV level by kriging interpolation. Then, the velocity magnitudes from the region of interest, for CFD and μ-PIV, are extracted and compared. SAS 9.2 (SAS Institute Inc., NC, USA) was used for nonparametric statistical computation and the computed P-value of the Kolomogorov-Smirnov test was 0.18. Since 0.18 is larger than 0.05, the null hypothesis is not rejected. As a result, at a 5% significance level, there is not sufficient evidence to support that CFD and PIV results are different.

4.4 Discussion

Limitations of the experiments on microvortices in a trapezoid side chamber are attributed to several factors. First, the quality and accuracy of μ -PIV results heavily depends on the tracing particles. Particles can experience both drag and lift forces in a microfluidic device (Carlo, 2009). However, with the long channel in the proposed design, drag forces are negligible when particles are accelerated to the speed of the flow. Moreover, lift forces are usually considered negligible when considering the low Reynolds numbers in our micro-fluidic devices. Some studies suggest that lateral inertial lift force and hydrodynamic lift force are imposed on the PIV tracing particles in microvortex systems and that those forces violate the assumption that the particles exert negligible impact on the fluid (Shelby & D. T. Chiu, 2003)(D. S. W. Lim, Shelby, Kuo, & D. T. Chiu, 2003). However, considering that the size of our trapezoid-chamber in our experiments is much larger than the size of tracing particles and that the microvortex region of interest is far from the side walls, we expect that the lift forces are negligible (Park et al., 2009). Furthermore, the particle concentration in the trapezoid-shape chamber is relatively low in our experiments, so the deformation of fluid induced by hydrodynamic lift force from particles is negligible. In conclusion, the effect of the particles is one of the fundamental problems in μ-PIV (*Particle Image Velocimetry a Practical Guide*, 2007), and there is no clear solution to this problem. More experiments are required to fully understand the effect on microvortex systems. Also, within any two-component μ-PIV study measuring the central plane only, the third component of the velocity profile is neglected.

For example, between two consecutive images, some particles may occur in the first frame but disappear in the second frame. Third, unlike the conventional PIV systems, μ-PIV systems do not use a light sheet and suffer from the presence of unfocused particles. Those out of focus particles cannot be removed since they are at the same wavelength as the signal (*Particle Image Velocimetry a Practical Guide*, 2007). Unfocused particles can generate bad vectors in PIV, which contribute to increases in average RMSE. Furthermore, PDMS possesses elastic material property and tends to enlarge itself when pressure inside of the device increases. As a result, this elasticity causes the ideal model of CFD conflict with the actual experiment. Lastly, the most challenging part of the μ-PIV experiment is the nonuniform distribution of particles inside the chamber. In some regions, the particle concentration is very low, and this deficiency leads to inaccuracy and low vector resolution. In order to ensure at least 5 particles even in low concentration regions, overall particle density was increased. However, with this process, the device suffered from particle aggregation at the lower right corner where the inner cavity and main channel connected, which might influence overall fluidic properties

Chapter 5

ROTATE A SINGLE CELL IN THE TRAPEZOID-SHAPE SIDE CHAMBER

The above studies were conducted with an absence of a single cell, and all works were based on the steady state assumption. As a result, the interaction between a single cell and a chamber, the motion of the cell before achieving steady state, and the feasibility of rotating the cell in a trapezoidal chamber were unknown. The answers to the above issues can be revealed by introducing real cells into the trapezoidal side chamber. Furthermore, to validate the capability of multiple-perspective imaging, a single cell that rotates around a fixed axis in the trapezoidal side chamber must be demonstrated.

5.1 Rotate polystyrene particles without external trapping

Mammalian cells are typically about 10 μm in diameter. In this study, 10 μm polystyrene particles were used, since they behaved similar to cells in fluidic condition. First, the 10 μm polystyrene particles were mixed with the 1 μm polystyrene particles with a ratio of 1:8. The 1 μm particles were used to visualize the trace of the flow while the recirculation was formed. The mixture was injected into a microfluidic device by a gear pump (milliGAT, GlobalFIA, WA, USA). After the entire channel was immersed by the mixture for several minutes, the microfluidic device was turned over to let the surface with the trapezoidal chamber face down. After settling for about one minute, by gravity force, one or more 10 μm polystyrene particles might be trapped inside of the trapezoidal side chamber. After selecting the chamber with only one 10 μm particle inside, a

volumetric flow rate of 0.02 μL was applied at the inlet. A CCD camera (Powerview Plus, TSI, MN, USA) captured the pictures in automatic exposure mode (32 frame/sec). Figure 5.1 demonstrates the movement of the particles.

In Figure 5.1, the 10 μm particle was initially located at the center of the trapezoidal chamber. Through observing the motion of the tracing particles, the flow in the main channel was from left to right, and the motion of the flow in the chamber was very slow. Looking at the first four pictures, the tracing particles in the upper part of chamber moved from right to left, and the tracing particles in the lower part of chamber moved in an opposite direction. Therefore, the flow motion in the trapezoidal side chamber was in a counterclockwise direction. Furthermore, the 10 μm particle slightly moved from left to right at the beginning. The bottom two pictures show that the 10 μm particle actually moved away from the vortex center, and then merged into the main flow. Finally, the 10 μm particle escaped from the field of view.

There are two constraints with this experiment. First, the 10 μm polystyrene bead used in this experiment was in perfect spherical shape, and it was very smooth without any mark on its surface. With this property, the single bead rotation was not able to be detected directly. Instead, the occurrence of rotation was indirectly observed by tracing the smaller particles. Second, the system was in accelerating states instead of a steady state. The microvortex trapping force was not enough to hold the particle. Therefore, during that time, the acceleration in the system dragged the 10 μm particle into the main flow. In order to solve the

above challenges, real cells were used, and the optical trapping system was introduced to provide external trapping force.

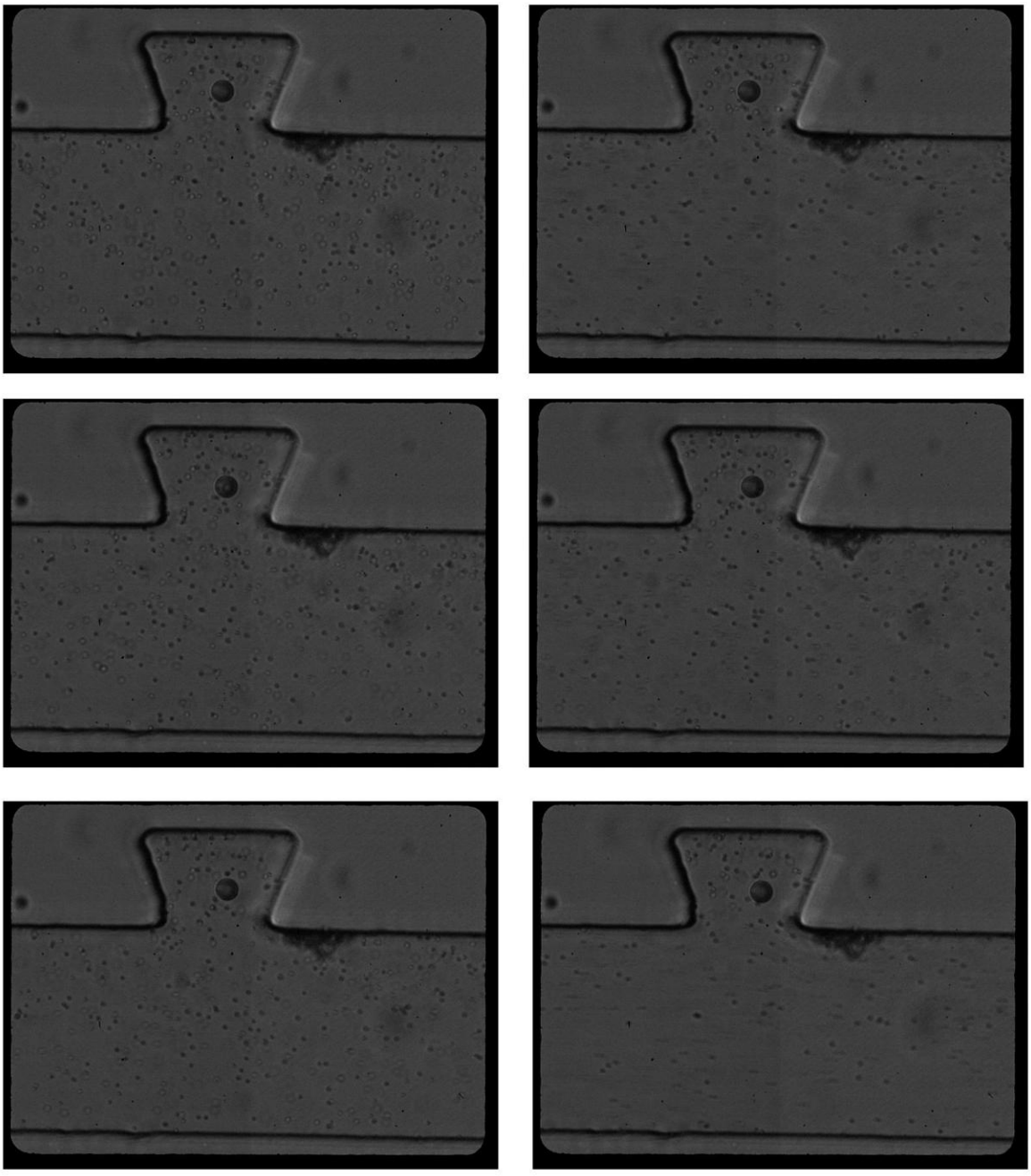

Figure 5.1. Micrographs of a 10 μm polystyrene bead in a trapezoid-shape side chamber with 1 μm tracing particles in different time frames

5.2 Rotate a single cell with optical trapping

5.2.1 Spherical cell rotation

This experiment of rotating a spherical shaped cell (CPC) was done by Andrew Shabilla, a student worker in CBDA. The experimental result is demonstrated in Figure 5.2. The optical trapping system was applied to transport a cell into the chamber and assist the cell rotation. (A) – (F) demonstrates the frames between 0 sec to 0.51 sec. In frame (A), a tiny bubble-looking spot was located at the 3 o'clock direction, and the motion of the entire object was estimated by tracing the spot position. In Figure 5.2, the single cell rotated around its center about 180 degrees after 0.51 sec. To calculate rotational rates, the video was transformed into images with a 0.033 sec/frame temporal resolution. Then, the position of one bubble-looking spot on the circumference was tracked. The period for this spot returning to its starting position was recorded, and then the RMP value was calculated. The calculated rotational rates ranged from 12 rpm to 29 rpm. One set of the images showed consistent rotation for 10 seconds, and the mean rotational rate was 24.9 ± 3.4 rpm.

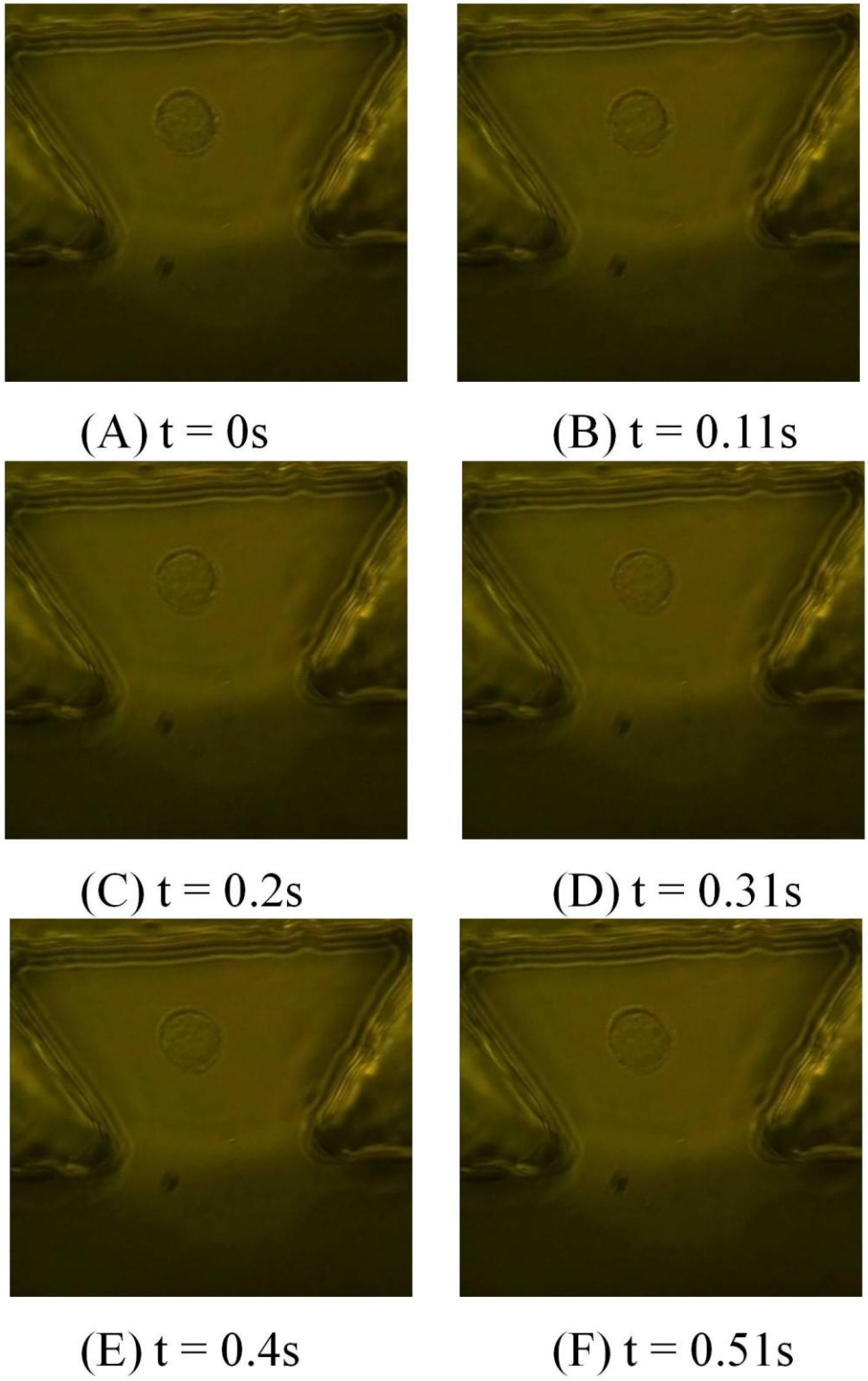

Figure 5.2. Micrographs of a single cell rotating 180 degrees in 0.51 sec

5.2.2 Irregular cell rotation

Some mammalian cells are not spherical in shape. Especially for cancer cells, they are deformed and irregular in shape. As a result, to ensure the capability of this device for rotating various types of cells, red blood cells (RBCs) were used for the experiments. RBCs are doughnut-shaped cells with an average diameter of 8 μm, and they are nonsymmetrical. Figure 5.3 sketches the cell rotation with respect to different time frames. A single RBC can be rotated around a fixed axis in a very stable manner. During the experiment, an RBC in the main channel was captured by optical tweezers and then moved into the chamber. The transverse pressure of the optical tweezers forced the RBC to stand on its side. As a result, the doughnut-shaped RBC was lifted up from the side by optical tweezers and viewed as rod-shaped. The trapping force was tested by moving the trapped cell around different locations quickly. Since the cell was not lost, the trapping force was considered strong enough. In Figure 5.3, the single RBC rotated in a clockwise direction. The vortex generated by the formation of the microvortex successfully rotated the RBC.

To calculate rotational rates, the video was transformed into images with a 0.033 sec/frame temporal resolution. Then, the position of one end of the rod shaped RBC was tracked. With a 0.5 μL/s flow rate, rotational rates were calculated by recording the required time for one end of the cell returning to its starting position. Computed rates ranged from 70 to 120 rpm. During a selected 40 second time interval while the rotation was consistent, mean rotational rate value was 97 ± 3 rpm. After increasing the flow rate, the rotational rate reached

an estimated 300 rpm or above. With strong optical trapping, a single RBC was not lost during the entire process of the experiment (20 minutes). The maximal rotational rate was determined by the maximal trapping force of the optical tweezers. The success of this experiment suggests that the trapezoidal side chamber is applicable to rotate non-spherical cells.

The mean irregular cell rotational rate was much higher than the regular cell rotational rate, because a higher flow rate was used to overcome strong resistances to rotation caused by the irregular shape. In this study, the applied flow rate ranged from 0.1 to 1 μL/s. When the flow rate was low, the cell swung about 40 degrees around the rotation axis with oscillation. When the flow rate was high enough, the cell began to rotate consecutively. However, step-wise rotation motion due to the irregular shape of the cell was also observed. The inhomogeneous rotation was caused by the off-centered rotation axis position. Therefore, the net torque exerted on a single cell was not constant.

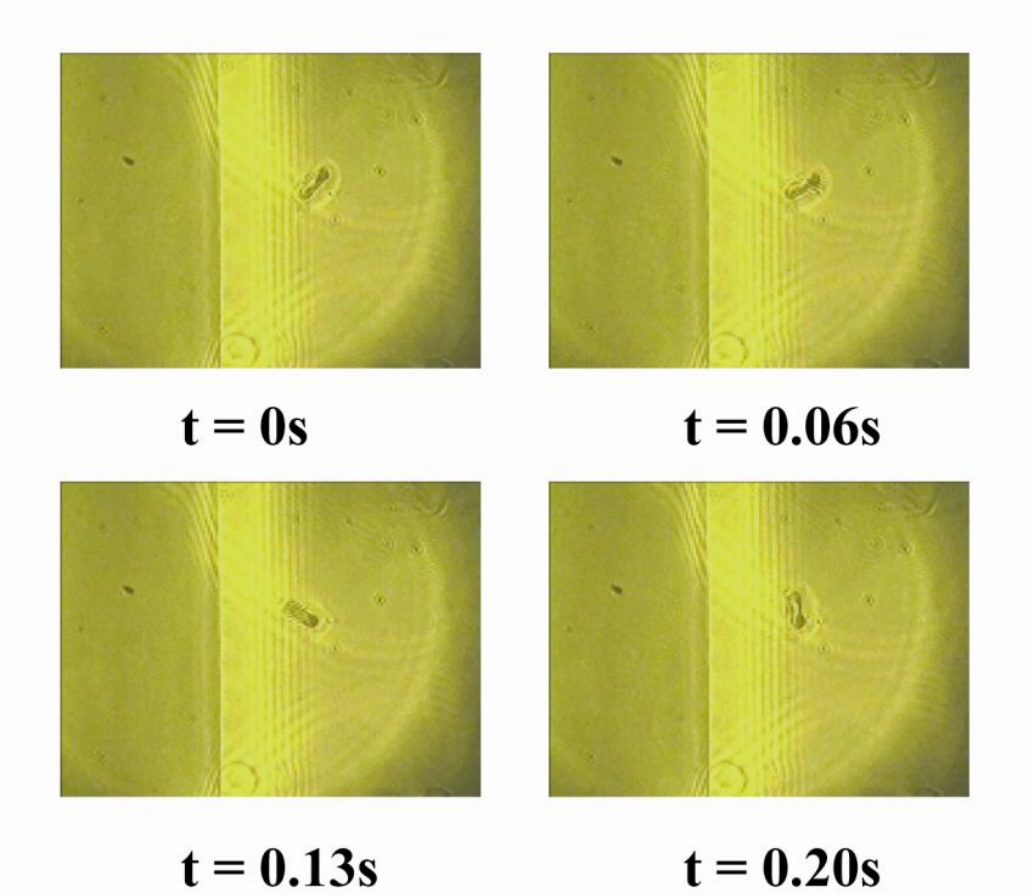

Figure 5.3. Micrographs of single RBC rotation from snapshots of movie frames with a frame rate of 17 frame/sec

It is believed that high shear stress induce both biological and morphological modification. Table 1 compares the shear stress inside of a trapezoidal side chamber with other conditions. With a 1 μL/s flow rate, the shear stress magnitude ranged from 0 to 6.5 dynes/cm^2. On the other hand, the main human arteries shear stress is about 2 – 20 dynes/cm^2 (Dewey, Bussolari, Gimbrone, & Davies, 1981). Cellular morphological elongation occurs when the shear stress is above 10 dynes/cm^2 (Ando & K. Yamamoto, 2009), G_2/M tumor cell cycle arrest occurs significantly when the exerted shear stress is above 12 dynes/cm^2 (S.-F.

Chang et al., 2008), and hemolytic damage starts when the shear stress is above 1500 dynes/cm^2 (Leverett, Hellums, Alfrey, & Lynch, 1972). Therefore, the shear stress inside of the trapezoidal side chamber is well controlled within suitable environment for living cells. Furthermore, the shear-induced responses are significantly expressed after treatment for more than 24 hours in many studies. However, for Cell CT applications, the required operation time is usually within several minutes. As a conclusion, the trapezoidal side chamber is unlikely to introduce significant biological or morphological changes.

	Shear Stress (dynes/cm^2)
Micro vortex in trapezoidal chamber	0 - 6.5
Major human arteries	2 - 20
Morphological elongation	>10
G_2/M cycle arrest	>12
Hemolytic damage	>1500

Table 1. Shear stress magnitude comparison among different biological conditions

Chapter 6

CONCLUSION

The trapezoidal side chamber provides great optical access and suitable environment for living cells. This chamber can rotate a single cell with controllable rate, which allows a successful imaging acquisition process for the cell CT system. Comparing with the previous capillary design, the trapezoidal side chamber provides better image quality and enables real time analysis with low cost feature.

The thesis work presented the pathway of designing the proposed trapezoidal side chamber with detailed optimization process by numerical simulations. The experimental approach constructed the flow profile within a trapezoidal side chamber, which has not been revealed by other studies. The feasibility of multiple-perspective imaging was validated by rotating both regular and irregular cells within the proposed chamber. The outcomes of the simulation parts are:

- Chamber opening affected the formation of microvortex. A chamber opening to a channel width ratio smaller than one was required for forming microvortex.
- Vorticity at the vortex center was directly proportional to the inlet velocity with a R^2 value higher than 99%.
- The trapezoidal side chamber was selected as the final design after comparing performance with rectangular and diamond side chambers because it provided the best optical access and high vortex center.

- Velocity distribution, vortex center height and vortex center vorticity values of trapezoidal side chambers were not sensitive to interface angles changes ranging from 0.32 to 0.64 rad.
- Velocity distribution, vortex center height and vortex center vorticity values of trapezoidal side chambers were not sensitive to the chamber heights, when the magnitude of the chamber height was significantly larger than the channel opening.

The achievements of the second parts are:

- The velocity profile was quantified with μ-PIV
- μ-PIV result matches with the CFD result with 95% confidence level

The results of the third part indicate:

- An external trapping device must be used because the trapping force produced by the microvortex was not enough to hold a single particle.
- The trapezoidal side chamber can rotate a regular-shape cell at the rate ranging from 12 to 29 rpm.
- The trapezoidal side chamber can rotate an irregular cell at a mean rate of 97 ± 3 rpm with a 0.5 μL/s flow rate.
- Shear stress within the trapezoid side chamber ranged from 0 to 6.5 dynes/cm^2, which is unlikely to modify cellular signaling.
- Rotation rates can be altered by changing flow rate.

Future works could include making an advanced CFD model by including both a single cell and optical trapping in the system. The μ-PIV experiment can be

improved by using smaller tracing particles and an advanced particles tracking algorithm. The robustness of the experimental flow profile could be increased by combing the optical trapping and μ-PIV systems together. A new design providing the feature of collecting the cells after rotation would facilitate downstream analysis.

REFERENCES

Ando, J., & Yamamoto, K. (2009). Vascular mechanobiology: endothelial cell responses to fluid shear stress. *Circulation Journal: Official Journal of the Japanese Circulation Society*, *73*(11), 1983-1992.

Arai, F., Kawaji, A., Luangjarmekom, P., Fukuda, T., & Itoigawa, K. (2001). Three-dimensional bio-micromanipulation under the microscope. *Robotics and Automation, 2001. Proceedings 2001 ICRA. IEEE International Conference on* (Vol. 1, pp. 604-609 vol.1).

Avery, S. V. (2006). Microbial cell individuality and the underlying sources of heterogeneity. *Nat Rev Micro*, *4*(8), 577-587.

Brehm-Stecher, B. F., & Johnson, E. A. (2004). Single-Cell Microbiology: Tools, Technologies, and Applications. *Microbiol. Mol. Biol. Rev.*, *68*(3), 538-559.

Carlo, D. D. (2009). Inertial microfluidics. *Lab on a Chip*, *9*(21), 3038-3046.

Chang, S.-F., Chang, C. A., Lee, D.-Y., Lee, P.-L., Yeh, Y.-M., Yeh, C.-R., Cheng, C.-K., et al. (2008). Tumor cell cycle arrest induced by shear stress: Roles of integrins and Smad. *Proceedings of the National Academy of Sciences*, *105*(10), 3927 -3932.

Chiu, D. (2007). Cellular manipulations in microvortices. *Analytical and Bioanalytical Chemistry*, *387*(1), 17-20.

Dewey, J., Bussolari, S. R., Gimbrone, J., & Davies, P. F. (1981). The Dynamic Response of Vascular Endothelial Cells to Fluid Shear Stress. *Journal of Biomechanical Engineering*, *103*(3), 177-185.

Eriksson, E., Enger, J., Nordlander, B., Erjavec, N., Ramser, K., Goksor, M., Hohmann, S., et al. (2007). A microfluidic system in combination with optical tweezers for analyzing rapid and reversible cytological alterations in single cells upon environmental changes. *Lab on a Chip, 7*(1), 71.

Fauver, M., Seibel, E., Rahn, J. R., Meyer, M., Patten, F., Neumann, T., & Nelson, A. (2005). Three-dimensional imaging of single isolated cell nuclei using optical projection tomography. *Optics Express, 13*(11), 4210-4223.

Fundamentals of Momentum, Heat, and Mass Transfer. (2001). (4th ed.). New York: Wiley.

Ha, J. B., Bahk, Y. K., Yoon, S. H., Lee, J. H., Jeong, E. H., Yoon, S. Y., Arakawa, T., et al. (2007). Microfludic Centrifuge of Nano Particles using Rotating Flow in a Microchamber. *Solid-State Sensors, Actuators and Microsystems Conference, 2007. TRANSDUCERS 2007. International* (pp. 927-930).

Leverett, L. B., Hellums, J. D., Alfrey, C. P., & Lynch, E. C. (1972). Red Blood Cell Damage by Shear Stress. *Biophysical Journal, 12*(3), 257-273.

Lidstrom, M. E., & Meldrum, D. R. (2003). Life-on-a-chip. *Nat Rev Micro, 1*(2), 158-164.

Lim, D. S. W., Shelby, J. P., Kuo, J. S., & Chiu, D. T. (2003). Dynamic formation of ring-shaped patterns of colloidal particles in microfluidic systems. *Applied Physics Letters, 83*(6), 1145.

Lin, C. M., Lai, Y. S., Liu, H. P., Chen, C. Y., & Wo, A. M. (2008). Trapping of Bioparticles via Microvortices in a Microfluidic Device for Bioassay Applications. *Analytical Chemistry, 80*(23), 8937-8945.

Liu, K., Pitchimani, R., Dang, D., Bayer, K., Harrington, T., & Pappas, D. (2008). Cell Culture Chip Using Low-Shear Mass Transport. *Langmuir, 24*(11), 5955-5960.

Loeb, L. A. (2003). Multiple mutations and cancer. *Proceedings of the National Academy of Sciences, 100*(3), 776-781.

Meyer, M. G., Fauver, M., Rahn, J. R., Neumann, T., Patten, F. W., Seibel, E. J., & Nelson, A. C. (2009). Automated cell analysis in 2D and 3D: A comparative study. *Pattern Recognition*, *42*(1), 141-146.

Miao, Q., Rahn, J. R., Tourovskaia, A., Meyer, M. G., Neumann, T., Nelson, A. C., & Seibel, E. J. (2009). Dual-modal three-dimensional imaging of single cells with isometric high resolution using an optical projection tomography microscope. *Journal of Biomedical Optics*, *14*(6), 064035.

Nandakumar, V., Kelbauskas, L., Johnson, R., & Meldrum, D. (2011). Quantitative characterization of preneoplastic progression using single-cell computed tomography and three-dimensional karyometry. *Cytometry Part A*, *79A*(1), 25-34.

Ota, H., Yamamoto, R., Deguchi, K., Tanaka, Y., Kazoe, Y., Sato, Y., & Miki, N. (2010). Three-dimensional spheroid-forming lab-on-a-chip using micro-rotational flow. *Sensors and Actuators B: Chemical*, *147*(1), 359-365.

Park, J.-S., Song, S.-H., & Jung, H.-I. (2009). Continuous focusing of microparticles using inertial lift force and vorticity via multi-orifice microfluidic channels. *Lab on a Chip*, *9*(7), 939-948.

Particle Image Velocimetry a Practical Guide. (2007). (2nd ed.). Heidelberg: Springer.

Qin, J. J., Yeo, L. Y., & Friend, J. R. (2009). MicroPIV and micromixing study of corona wind induced microcentrifugation flows in a cylindrical cavity. *Microfluidics and Nanofluidics*, *8*(2), 231-241.

Santiago, J. G., Wereley, S. T., Meinhart, C. D., Beebe, D. J., & Adrian, R. J. (1998). A particle image velocimetry system for microfluidics. *Experiments in Fluids*, *25*(4), 316-319.

Schmid, A., Kortmann, H., Dittrich, P. S., & Blank, L. M. (2010). Chemical and biological single cell analysis. *Current Opinion in Biotechnology*, *21*(1), 12-20.

Shelby, J. P., & Chiu, D. T. (2003). Mapping Fast Flows over Micrometer-Length Scales Using Flow-Tagging Velocimetry and Single-Molecule Detection. *Analytical Chemistry*, *75*(6), 1387-1392.

Shelby, J. P., & Chiu, D. T. (2004). Controlled rotation of biological micro- and nano-particles in microvortices. *Lab on a Chip*, *4*(3), 168. doi:10.1039/b402479f

Shelby, J. P., Lim, D. S. W., Kuo, J. S., & Chiu, D. T. (2003). Microfluidic systems: High radial acceleration in microvortices. *Nature*, *425*(6953), 38.

Shelby, J. P., Mutch, S. A., & Chiu, D. T. (2004). Direct Manipulation and Observation of the Rotational Motion of Single Optically Trapped Microparticles and Biological Cells in Microvortices. *Analytical Chemistry*, *76*(9), 2492-2497.

Suresh, S., Spatz, J., Mills, J. P., Micoulet, A., Dao, M., Lim, C. T., Beil, M., et al. (2005). Connections between single-cell biomechanics and human disease states: gastrointestinal cancer and malaria. *Acta Biomaterialia*, *1*(1), 15-30.

Yamakoshi, Y., & Noguchi, Y. (1998). Micro particle trapping by opposite phases ultrasonic travelling waves. *Ultrasonics*, *36*(8), 873-878.